Timms, N.E. and Erickson, T. and Zanetti, M. and Pearce, M. and Cayron, C. and Cavosie, A. and Reddy, S. et al. 2017. Cubic zirconia in >2370 °C impact melt records Earth's hottest crust. Earth and Planetary Science Letters. 477: pp. 52-58.

Cubic zirconia in >2370 °C impact melt records Earth's hottest crust

Nicholas E. Timms[1]*, Timmons M. Erickson[1], Michael R. Zanetti[2], Mark A. Pearce[3], Cyril Cayron[4], Aaron J. Cavosie[1,5], Steven M. Reddy[1], Axel Wittmann[6], Paul K. Carpenter[7]

[1] Department of Applied Geology, Curtin University, Perth, GPO Box U1987, Western Australia 6845, Australia

[2] University of Western Ontario, 1151 Richmond St, London, Ontario, Canada N6A 3K7

[3] CSIRO Mineral Resources, Australian Resources Research Centre, 26 Dick Perry Avenue, Kensington, WA 6151, Australia

[4] Laboratory of ThermoMechanical Metallurgy (LMTM), PX Group Chair, École Polytechnique Fédérale de Lausanne (EPFL), Rue de la Maladière 71b, 2000 Neuchâtel, Switzerland

[5] NASA Astrobiology Institute, Department of Geoscience, University of Wisconsin-Madison, Madison WI, USA

[6] LeRoy Eyring Center for Solid State Science, Arizona State University, 901 S Palm Walk, Tempe, AZ, 85287, USA

[7] Washington University in St Louis, Earth and Planetary Science Department and the McDonnell Center for Space Sciences; 1 Brookings Drive, St Louis MO, 63112, USA

*Corresponding author email: n.timms@curtin.edu.au

Cubic zirconia in >2370 °C impact melt records the hottest crust on Earth

Highlights

- Zircon has partially dissociated in impact melt rock from a Canadian impact crater
- Former presence of cubic ZrO_2 is crystallographically encoded in reaction rims
- Cubic zirconia required >2370 °C melt, which is hottest recorded on Earth's surface
- Such superheated melt susceptible to devolatilization resulting in dry rigid crust
- Potential global effects for crustal evolution during bombardment of early Earth

ABSTRACT

Bolide impacts influence primordial evolution of planetary bodies because they can cause instantaneous melting and vaporization of both crust and impactors. Temperatures reached by impact-generated silicate melts are unknown because meteorite impacts are ephemeral, and established mineral and rock thermometers have limited temperature ranges. Consequently, impact melt temperatures in global bombardment models of the early Earth and Moon are poorly constrained, and may not accurately predict the survival, stabilization, geochemical evolution and cooling of early crustal materials. Here we show geological evidence for the transformation of zircon to cubic zirconia plus silica in impact melt from the 28 km diameter Mistastin Lake crater, Canada, which requires super-heating in excess of 2370 °C. This new temperature determination is the highest recorded from any crustal rock. Our phase heritage approach extends the thermometry range for impact melts by several hundred degrees, more closely bridging the gap between nature and theory. Profusion of > 2370 °C superheated impact melt during high intensity bombardment of Hadean Earth likely facilitated consumption of early-formed crustal rocks and minerals, widespread volatilization of various species, including hydrates, and formation of dry, rigid, refractory crust.

KEYWORDS: cubic zirconia, zircon, phase transformation, impact melt, planetary evolution, early Earth

1. INTRODUCTION

Shock wave propagation during hypervelocity impact can melt and vaporize both the impactor and target rocks (Melosh, 1989). The immediate, post-impact, thermal pulse far exceeds both ultra-high-temperature metamorphism in tectonic settings (Heisinger and Head, 2006; Korhonen et al., 2014) and the liquidus temperatures of target rocks, and is therefore important for the evolution of planet and asteroid surfaces. The heat associated with impacts had a profound significance on the early Earth, and has been shown to have affected processes in Earth's core (Arkani-Hamed and Ghods, 2011; Monteux et al., 2015; Sleep, 2016), mantle (Watters et al., 2009), crust and atmosphere (Marchi et al., 2016; Marchi et al., 2014; Marchi et al., 2013; Melosh, 2008).

Volatile depletion and isotope fractionation of Earth, Moon and other planetary bodies are attributed to giant basin-forming impacts (Albarede et al., 2013; Day and Moynier, 2014; Moynier et al., 2010; Pringle et al., 2014). Vaporization of target and impactor material during impacts is temperature dependant. Preferential mass-dependant volatile loss and isotope fractionation from impact melts can therefore locally influence subsequent remelting and rheological behaviour, and so giant impacts and/or the cumulative effects of intense periods of impact bombardment have important geodynamic consequences (Albarede, 2009). These effects, in turn, have implications for the evolution and habitability of Earth's surface environment (Abramov and Mojzsis, 2009; Ryder, 2002), and, by extension, the habitability of extraterrestrial planetary bodies and exoplanets.

Initial thermal properties of impact melt also control their ability to digest pre-existing solid material and entrained debris (Onorato et al., 1978), including metals and sulphides essential for forming impact-generated economic ore deposits (Keays and Lightfoot, 2004), their cooling rate (Onorato et al., 1978), and consequently the preservation of all pre-existing material and high-P phases formed during the passage of the shock wave (Tschauner et al., 2014). The highest temperature superheated melts (i.e., above the liquidus - the equilibrium temperature for complete melting) and vapor are produced during shock-release melting and frictional melting, whereas exhumation-related decompression melting is limited to sub-liquidus temperatures (Ahrens and O'Keefe, 1971; French and Koeberl, 2010; Melosh, 1989; Melosh, 2005; Riller et al., 2010; Spray, 1998).

The critical melting temperature of target rocks depends on their composition, proximity to the impact site, initial conditions (Gibbons et al., 1975; Hörz et al., 2005; Stöffler, 1971) and porosity (Kieffer et al., 1976; Wünnemann et al., 2008). Vaporization temperature is taken as the highest vaporization temperature of oxides present in the system; in real systems, incongruent vaporization may occur over a range of temperatures (Ahrens and O'Keefe, 1971; Grieve et al., 1977; Lamoreaux et al., 1987; Lou et al., 1985). However, the complex behaviour of silicates has made shock-related heating and, thus, the magnitudes of impact melt superheating and vaporization difficult to predict with any degree of certainty (Ahrens and O'Keefe, 1971). Accordingly, our understanding of temperatures achieved by impact melts necessarily relies on empirical constraints from the rock record via established geothermometers, which have inherently limited temperature ranges (Asimow and Ghiorso, 1998; Cherniak et al., 2007; Hart and Davis, 1978; Kubaschewski, 1982; Lindsley and Andersen, 1983; Sack and Ghiorso, 1991; Taylor et al., 2015). As there are large ranges between liquidus and vaporization temperatures for most rock types, maximum impact melt temperatures are largely unaccounted for, thus the effects of superheated melt may be underappreciated in planetary surface studies.

In the rock record, glass spherules and some types of microtektites contained within impact ejecta horizons provide *a priori* evidence for atmospheric condensation of silicate vapor (Glass and Simonson, 2012). In rare cases, nickel-rich magnesiowüstite inclusions in spherules indicate condensation temperatures >2300 °C (Kyte and Bohor, 1995). However, no direct geological evidence has been reported for high temperatures in contiguous impact melt rock, quenched ejected melt droplets (tektites), or impact melt-bearing breccia (suevite) because no geothermometers applicable to impact melt are calibrated beyond ~2000 °C (Asimow and Ghiorso, 1998; Cherniak et al., 2007; Hart and Davis, 1978; Kubaschewski, 1982; Lindsley and Andersen, 1983; Sack and Ghiorso, 1991; Taylor et al., 2015). Furthermore, models of impact melt formation often assume initial melt temperatures of ~1700 °C (Abramov et al., 2013; Onorato et al., 1978; Simonds, 1975), and in some cases allude to temperatures >2000 °C (Wünnemann et al., 2008).

In this study, we investigate the microstructure of zirconia (ZrO_2) produced during the dissociation of zircon ($ZrSiO_4$) in impact glass (quenched impact melt) sampled from the 28-km-diameter, 37.83 ± 0.05 Ma Mistastin Lake impact structure in northern Labrador, Canada (55°53’N; 63°18’W) (Marion and Sylvester, 2010; Sylvester et al., 2013). We present new thermometry based on reconstruction of the polymorphic transformation history of zirconia in a reaction rim around a zircon grain, an approach we refer to as phase heritage. Crystallographic relationships reveal the former presence of cubic zirconia, which definitively quantifies the minimum impact melt temperature to > 2370 ºC, far exceeding commonly assumed impact melt temperatures. These results thus present fundamental new constraints on the evolution of impact melts, and influence our understanding of the evolution of early planetary crust, when impact rates were orders of magnitude higher than now, substaintial resurfacing by impact structures comparable to or larger in size than Mistastin Lake occurred (Marchi et al., 2014; Morbidelli et al., 2012), and all physical evidence of cratering was subsequently destroyed.

2. METHODS AND APPROACH

We characterised the zircon grain and surrounding area *in situ* on a polished thin section with cathodoluminescence (CL), backscattered electron (BSE) imaging and wavelength dispersive spectroscopy (WDS). We used electron backscatter diffraction (EBSD) to verify the mineral assemblage and characterize and quantify the crystallographic orientation and microstructure of zirconia (ZrO_2) produced by the dissociation of zircon ($ZrSiO_4$). See Supplementary File for further information about data acquisition and processing. Crystallographic relationships among zirconia grains preserve the phase transformation history, or phase heritage, of zirconia polymorphs (Cayron et al., 2010; Kerschhofer et al., 2000). Transformations between mineral phases commonly occur with systematic crystallographic orientation relationships (e.g., Pearce et al., 2013). New phases tend to nucleate at multiple sites in one of several symmetrically equivalent orientations. The new grain orientations in the resulting polycrystalline microstructure are related by systematic misorientations, described by specific angular rotations around specific crystallographic axes that are strictly controlled by the symmetry relationships between the old and new phases. Therefore, the original (parent) crystal orientation can be inferred by combining the misorientations between the new (daughter) phase grains and the transformation relationships, even when the old crystal has been completely transformed. This concept of orientation-based phase heritage has been used to identify the former presence of high-temperature zirconia polymorphs in manufactured ceramics (Cayron et al., 2010; Chevalier et al., 2009) and kimberlites (Kerschhofer et al., 2000), and the high-pressure $ZrSiO_4$ polymorph reidite in impactites (Cavosie et al., 2016; Timms et al., 2017), and we use it here to investigate the thermal evolution of zircon entrained into impact melt.

The orientation relationships (OR) for the transformations from cubic-tetragonal-monoclinic zirconia due to cooling are well known from the literature on refractory ceramics, and measured orientations of low-temperature monoclinic zirconia (baddeleyite) can be used to reconstruct orientations of parent cubic grains, the highest temperature zirconia polymorph (Cayron, 2007; Cayron et al., 2010). This approach relies on $\langle a\rangle_{cubic} \rightarrow \langle a\rangle_{tetragonal}$ or $\langle c\rangle_{tetragonal}$, generating up to three possible unique tetragonal orientations from a single cubic grain. During subsequent tetragonal-monoclinic transformation upon further cooling, the following transformation rules apply:

$\langle a\rangle_{tetragonal}$ or $\langle c\rangle_{tetragonal} \rightarrow \langle b\rangle_{monoclinic}$

plus either

$\langle a\rangle_{tetragonal}$ or $\langle c\rangle_{tetragonal} \rightarrow \langle a\rangle_{monoclinic}$ (type 1 OR after Cayron et al., 2010)

or

$\langle a\rangle_{tetragonal}$ or $\langle c\rangle_{tetragonal} \rightarrow \langle c\rangle_{monoclinic}$ (type 2 OR after Cayron et al., 2010)

allowing for up to four unique orientation variants from each tetragonal identity (Chevalier et al., 2009), totalling twelve possible monoclinic variants from a single cubic identity (Cayron et al., 2010).

The Python-based software combination of ARPGE and GenOVa were used to perform a crystallographic orientation analysis of baddeleyite (monoclinic zirconia) to reconstruct evidence for precursor zirconia polymorphs following the approach applied by Cayron (2007) and Cayron et al. (2010) for ceramic applications. This method automatically and objectively reconstructs ‘parent’ grains using known sets of orientation relationships among ‘daughter’ grains that have been established to result from phase transformations between specific zirconia polymorphs.

3. RESULTS

The zircon grain analyzed, MZRN-1, is in a glassy impact melt rock, exposed on top of the 80 m thick columnar jointed impact melt body at Discovery Hill near the crater wall (Marion and Sylvester, 2010). Mistastin impact melt rock composition ranges from ~53 to ~59 wt % SiO_2 and is interpreted to reflect mixing of different proportions of various crystalline igneous target rocks (Marion and Sylvester, 2010). Field relations indicate the melt ponded at Earth’s surface at ambient atmospheric pressure (Marion and Sylvester, 2010). The zircon records a pre-impact U-Pb crystallization age of 1403 +/- 10 Ma (2σ error, n = 3, MSWD = 0.85), consistent with derivation from Mesoproterozoic bedrock in the region (Zanetti, 2015). Other phases in the matrix include ballen-textured silica, which is also characteristic of high-temperature (>1200 °C) impact melt (Ferrière et al., 2009).

Zircon grain MZRN-1 has an oscillatory zoned core in cathodoluminescence (CL) that is truncated by a ~2 μm wide, bright CL rim that contains zirconia particles with interspersed sub-μm silicate melt inclusions (Fig. 1). The grain is cut by irregular fractures and contains two voids, all filled with glassy silicate impact melt (Fig. 1B). The zircon does not preserve any diagnostic shock-deformation microstructures, such as twins or the high-pressure $ZrSiO_4$ polymorph reidite (Timms et al., 2017) (Supplementary File item 2). Minor lattice misorientations (<5°) are associated with rigid block rotation across brittle fractures (Supplementary File item 2), but in general the core of the zircon appears undeformed.

The core is surrounded by a ~40 μm thick corona of vermicular ZrO_2 crystals ranging from ~0.5 to ~5 μm across and up to ~20 μm long (Fig. 1). Elongate crystals tend to be aligned at high angles to the zircon core, and form domains of morphologically similar clusters up to ~50 μm wide. Individual crystals generally do not impinge on each other, and are separated by glassy silicate impact melt similar in composition to the surrounding crystal-free impact melt (Fig. 1). ZrO_2 contains lower trace elements abundances (e.g., ~350 ppm Ti, ~275 ppm Th, ~90 ppm Y) than zircon (e.g., ~900 ppm Ti, ~600 ppm Th, ~1900 ppm Y) (Supplementary File item 4). Most (>99%) of the ZrO_2 grains index as baddeleyite (monoclinic ZrO_2). No crystalline SiO_2 phases were detected (Figs 1, 2).

Baddeleyite grains are commonly twinned and have a wide range of crystallographic orientations (Fig. 2A, C). Morphologically distinct clusters of baddeleyite grains preserve up to twelve unique crystallographic orientation variants with a systematic relationships among them (Fig. 2D, Supplementary File item 5). Groups of grains are crystallographically orientated approximately orthogonal to one another, and systematic deviations from orthogonality of ~20° form cross-shaped patterns on pole figures of <100> (Fig. 2D).

The occurrence of spatially-clustered baddeleyite grains with these distinctive patterns of twelve orientations uniquely identifies the former presence and orientation of a precursor cubic zirconia polymorph from the two-stage transformation from cubic to tetragonal to monoclinic zirconia (Fig. 2B, E) (Cayron et al., 2010). Initial processing of the EBSD maps of MZRN-1 involved dilation of daughter monoclinic zirconia grains by an iterative nearest neighbour extrapolation routine so that they impinge on one another (Supplementary File Fig. S3). This was required in order to perform neighbour-pair disorientation analysis within the ARPGE software.

Observed peaks we identified in disorientation analysis of MZRN-1 at 90°, 115°, and 180° are consistent with cubic-monoclinic transformation twinning (Fig. 3). We identified symmetry operators for disorientations between daughter monoclinic zirconia grains at these specific angles in crystal reference frame (Fig. 3).

We used the software GenOVa to develop a list of theoretical symmetry operators for the cubic-monoclinic transformation according to OR type 1 or type 2 OR (Cayron et al., 2010) to reconstruct the parent cubic zirconia grains (Figs 2, 3). Parent grain reconstruction involved a quadruplet search method with a minimum of five daughter grains per parent grain (Cayron et al., 2010). The disorientations we observed (angles +axes) fit very well with rotations by the operators expected from OR type 2, within an angular tolerance range of <5 ° (Fig. 3). We conclude that OR type 2 is the OR in the samples: there is no evidence that OR type 1 is present. The observed spread of the orientations (Fig. 3) is not due to a mixture of OR types 1 and 2, and may be due to limited crystal-plasticity in the dynamic impact melt environment. We used 15-20° as the tolerance angle for the parent cubic grain reconstruction (Fig. 2B, D, Supplementary File Fig. S5).

Reconstruction of parent cubic zirconia grains from baddeleyite electron backscatter diffraction (EBSD) data shows that the dissociation corona was once comprised of large (~5 to ~50 μm across) domains of vermicular single crystals of cubic zirconia (Fig. 2B). The morphology of the cubic parent grains indicates that the vermicular ZrO_2 grains formed a connected 3D network that broadly pseudomorphed the original rim of the zircon grain. A second zircon from the same sample (MZRN-2) displays the same partial dissociation texture and also successfully yields reconstructed parent cubic zirconia grains (Supplementary File items 3 and 5), indicating the same cubic zirconia phase heritage as MZRN-1.

4. DISCUSSION

The microstructural and geochronological data, field relations, and thermodynamic constraints all support the interpretation that the zircon grains described here record an extreme high-temperature history at low-pressure conditions. The Mesoproterozoic U-Pb age and preserved igneous zoning of MZRN-1 indicate that the grain is a xenocryst derived from one of the plutonic igneous target rocks. The complete lack of crystal-plastic deformation, shock-twins and high-pressure polymorphs are consistent with the grains not having been affected by high-pressure shock conditions. The grains were, however, entrained into impact melt in the dynamic crater environment after passage of the shock wave. The ZrO_2 coronae are therefore interpreted to have developed solely due to thermal effects from immersion in super-heated impact melt at ambient pressure. The inference of ambient pressure is also consistent with available thermodynamic constraints that indicate that the zircon dissociation reaction line has a steep Clapeyron slope (29 °C/bar) and therefore is inevitably a low-pressure process (Timms et al., 2017).

A minimum temperature achieved by the impact melt can be constrained via analysis of phases in the zirconia corona, and we use the ZrO_2-SiO_2 binary phase diagram at 1 atm to establish the temperature of zircon dissociation (Fig. 4) (Kaiser et al., 2008). The presence of a thick zirconia corona clearly records the melt achieving high enough temperature for zircon dissociation to proceed (Fig. 4) (Kaiser et al., 2008). Phase equilibria predict that zircon dissociates to tetragonal zirconia and cristobalite at 1673 °C (Fig. 4). The presence of silicate melt and absence of cristobalite indicates the sample exceeded 1687 °C; liquid silica released by dissociation would have dissolved into surrounding melt.

Clusters of morphologically distinct zirconia crystals that contain up to twelve unique orientations with systematic misorientations are consistent with a two-stage solid-state transformation from cubic zirconia via tetragonal zirconia. The former presence of cubic zirconia requires that the zircon, and therefore the melt that surrounds it, reached a minimum temperature of 2370 °C, but did not exceed 2700 °C above which cubic zirconia would have melted (Fig. 4), and thus prevented crystallographic phase heritage relations from being preserved. Upon cooling below 2370 °C, the displacive transformation of cubic to tetragonal zirconia results in up to three distinct orientations of tetragonal zirconia whereby $(001)_{tetragonal}$ is parallel to a $\{100\}_{cubic}$ (Heuer, 1987). Further cooling below ~1180 °C results in a stable assemblage of baddeleyite + zircon (Fig. 4). The tetragonal –monoclinic zirconia transformation is martensitic, and resulted in four orientation variants of baddeleyite from each tetragonal parent (Cayron et al., 2010). Thus, the transformation of higher-temperature cubic ZrO_2 polymorphs in the corona to the low temperature ZrO_2 polymorph baddeleyite produced systematic orientation relationships among baddeleyite grains. These are interpreted as transformation (reversion) twins formed upon cooling (Supplementary File item 6).

Even though cubic zirconia is the highest temperature ZrO_2 polymorph, its stability is pressure-dependant, such that it is stabilized at lower temperature with increasing pressure (Bouvier et al., 2000; Kerschhofer et al., 2000) (Supplementary File item 7). However, zirconia in the Mistastin sample is a product of zircon dissociation, which ostensibly is a low-pressure phenomenon that occurs at post-shock conditions (see Timms et al., 2017for further details and thermodynamic calculations). All available field evidence, theoretical constraints, microstructural and geochemical data supports zircon dissociation in an unconfined impact melt at ambient, post-shock pressure. Therefore, the transformations among zirconia polymorphs that took place after zircon dissociation necessarily also occurred in the melt sheet at post-shock low-pressure conditions, which constrains the stability of cubic zirconia to extremely high temperatures. Impurities, such as REE and Y, can also stabilize cubic zirconia at lower temperatures (Swab, 2001) (Supplementary File item 7). However, the levels of trace elements present in the ZrO_2 are much less than 0.1 wt% (Supplementary File item 4), and so the effects of impurities on the cubic to tetragonal zirconia transformation temperature were negligible (Swab, 2001) (Supplementary File item 7). Therefore, the former presence of cubic zirconia in the Mistastin Lake zircon indicates that the impact melt temperature was in excess of 2370 °C (Fig. 3) (Kaiser et al., 2008).

Our study documents forensic geological evidence for a minimum temperature of 2370 °C in a sample of impact melt. This temperature constraint is the highest recorded by any rock on Earth's surface, and is several hundred degrees higher than previous estimates for average temperatures of superheated impact melts (Fig. 5) (Onorato et al., 1978; Simonds, 1975; Wünnemann et al., 2008).

The ability to assess the phase heritage of ZrO_2 polymorphs by crystallographic orientation relationships is a new methodology for establishing the thermal evolution of superheated melt. Textural evidence of zircon dissociation and associated zirconia has been reported in numerous examples, including impact melt rocks, tektites, lunar melt breccias, kimberlites, as well as anthropogenic settings, such as slag from metal smelting and nuclear test sites (Timms et al., 2017). Given that zircon is a common accessory mineral in many rocks, this approach can be used to assess minimum temperatures of zircon-bearing impact melt rocks from Earth, Moon, and meteorites. The broader use of determining phase heritage can potentially be applied to a wide range of polymorphic transformations in geological systems.

Our results begin to constrain the conditions under which zircon and its U-Pb isotope systematics may survive during impact cratering. During high temperature and low shock pressure events, zircon is capable of surviving extreme conditions without necessarily recording microstructural evidence typical of shock deformation (Erickson et al., 2017; Timms et al., 2017; Timms et al., 2012). The Mesoproterozoic U-Pb protolith zircon age preserved in the ~38 Ma impact melt investigated here indicates that, despite being entrained in impact melt in excess of 2370 °C, the residence time at high temperature was not sufficient to cause significant Pb-loss from the core of the grain by volume diffusion (Cherniak and Watson, 2001). The glassy matrix is further evidence that duration at extremely high temperatures was short and the sample quenched rapidly. However, increased melt volumes in larger impact structures with slower cooling rates may lead to complete digestion of zircon xenocrysts, erasing mineralogical evidence of superheated temperatures. Early during Earth's history when impact rates were high, digestion of zircon by superheated impact melt may have contributed to the paucity of Hadean zircon preserved in the geological record (Marchi et al., 2014).

The formation of >2370 °C impact melt during moderate sized impacts has several significant, global-scale consequences during the early evolution of the Earth and Moon when the frequency and magnitude of meteorite flux was much higher (Gomes et al., 2005; Kring and Cohen, 2002). The extent of compositional modification by differential volatile loss of major and trace elements from impact melts by selective vaporization at temperatures >2370 °C has not been fully investigated, yet are sufficiently high to cause significant volatilization of many key oxide constituents of silicate melts (Lamoreaux et al., 1987). Preferential volatilization of SiO_2, Na_2O and K_2O components from hot impact melt bodies could provide a mechanism for localised densification of residual crust, potentially with geodynamic consequences. Molecular species essential for terrestrial life, such as H_2O and CO_2, are potentially lost due to volatilization of superheated impact melt. High-temperature impact-melting could locally form dry, rigid, refractory residual crust, resistant to subsequent melting. Moderate sized impacts, comparable to Mistastin, are predicted to have completely resurfaced the Earth within the first tens of millions of years after the Moon-forming event, irrespective of the choice of the suggested bombardment models (Marchi et al., 2014). Therefore, the resultant net effect of hypothesised high impact flux early during Earth's history, combined with commonplace high temperatures of impact melts, potentially led to widespread depletion of hydrous minerals from the lithosphere and therefore governed rheological properties of early crust. Further investigation of the geodynamic consequences of this phenomenon for early Earth would require accurate predictions of impact melt temperatures, flux, size, impact angles, and velocity distributions of impactors, and appropriate scaling relationships for melt volumes linked to these variables. Furthermore, long term effects would need to account for rehydration effects by interaction with Earth's hydrosphere. Our results on high temperature melt and attendant volatilization processes have implications for the early evolution of the geochemical reservoirs and multi-element isotope systematics of planetary bodies (Drake and Righter, 2002) and that extremely high melt temperatures can be achieved even in moderate-sized impact events, and are not limited to giant, basin-forming impacts.

FIGURE CAPTIONS

Figure 1. A. Panchromatic cathodoluminescence (CL) image of zircon (Zrn) xenocryst with a corona of baddeleyite (Bdy) and silicate glass. B. Backscattered electron image of area shown by white box in A showing the zircon-baddeleyite-glass interface.

Figure 2. A. Electron backscatter diffraction map coloured for measured crystallographic orientation of baddeleyite. Zircon is shown in grayscale based on EBSD pattern quality (band contrast). B. Map showing crystallographic orientations of reconstructed parent cubic zirconia grains. Inverse pole figure (IPF) orientation colour scheme. C-F. Pole figures showing measured 'daughter' baddeleyite orientations and reconstructed cubic zirconia 'parent' orientations. Lower hemisphere plots in sample x-y-z reference frame.

Figure 3. Results from orientation analysis of daughter monoclinic zirconia grains of MZRN-1 using the software ARPGE (Cayron, 2007; Cayron et al., 2010). A. Histogram of disorientation angles between daughter monoclinic grains. B. Disorientation symmetry operator statistics for adjacent daughter grains for operators for the type 2 orientation relationship (OR) of Cayron et al. (2010). C. Pole figures showing the distribution of 90°, 115°, and 180° disorientation axes between daughter grains in the crystal reference frame.

Figure 4. T-X phase diagram for ZrO_2-$ZrSiO_4$-SiO_2 system modified after Kaiser et al. (2008). Tridymite stability after Swamy et al. (1994). Crosshatch shows zircon-bearing fields, stipple shows melt-bearing fields.

Figure 5. Ranges for various types of high-temperature thermometers available in geosciences. Cubic zirconia (blue bar) related to zircon dissociation (blue arrow) is the thermometer for highest known temperatures (numbers on left indicate references). Vaporization field is approximate and based on rates for common species present in silicate melts (Lamoreaux et al., 1987).

ACKNOWLEDGEMENTS

M.Z. acknowledges support from a Barringer Family Award for Impact Cratering Research, a Mineralogical Society of America Petrology Research Grant, a Eugene M. Shoemaker Award for Impact Crater Research, and a Meteoritical Society Travel Grant (NASA Cosmochemistry Program). A.J.C. acknowledges support from a Curtin Research Fellowship and a NASA Astrobiology Grant. S.M.R. and T.M.E acknowledge the ARC Core to Crust Fluid Systems C.o.E. for research support. S. Marchi and S. Mojzsis are acknowledged for their constructive reviews of the manuscript, and J. Brodholt is thanked for editorial handling.

REFERENCES

Abramov, O., Kring, D.A., Mojzsis, S.J., 2013. The impact environment of the Hadean Earth. Chemie der Erde - Geochemistry 73, 227-248.

Abramov, O., Mojzsis, S.J., 2009. Microbial habitability of the Hadean Earth during the late heavy bombardment. Nature 459, 419-422.

Ahrens, T.J., O'Keefe, J.D., 1971. Shock melting and vaporization of lunar rocks and minerals, Conference on Lunar Geophysics, Lunar Science Institute, Houston, USA, pp. 214-249.

Albarede, F., 2009. Volatile accretion history of the terrestrial planets and dynamic implications. Nature 461, 1227-1233.

Albarede, F., Ballhaus, C., Blichert-Toft, J., Lee, C.T., Marty, B., Moynier, F., Yin, Q.Z., 2013. Asteroidal impacts and the origin of terrestrial and lunar volatiles. Icarus 222, 44-52.

Arkani-Hamed, J., Ghods, A., 2011. Could giant impacts cripple core dynamos of small terrestrial planets? Icarus 212, 920-934.

Asimow, P.D., Ghiorso, M.S., 1998. Algorithmic modifications extending MELTS to calculate subsolidus phase relations. American Mineralogist 83, 1127-1132.

Bouvier, P., Djurado, E., Lucazeau, G., Le Bihan, T., 2000. High-pressure structural evolution of undoped tetragonal nanocrystalline zirconia. Physical Review B 62, 8731-8737.

Cavosie, A.J., Timms, N.E., Erickson, T.M., Hagerty, J.M., Hörz, F., 2016. Transformations to granular zircon revealed: Twinning, reidite, and ZrO_2 in shocked zircon from Meteor Crater. Geology 44, 703-706.

Cayron, C., 2007. ARPGE: a computer program to automatically reconstruct the parent grains from electron backscatter diffraction data. Journal of Applied Crystallography 40, 1183-1188.

Cayron, C., Douillard, T., Sibil, A., Fantozzi, G., Sao-Jao, S., 2010. Reconstruction of the Cubic and Tetragonal Parent Grains from Electron Backscatter Diffraction Maps of Monoclinic Zirconia. Journal of the American Ceramic Society 93, 2541-2544.

Cherniak, D.J., Manchester, J., Watson, E.B., 2007. Zr and Hf diffusion in rutile. Earth and Planetary Science Letters 261, 267-279.

Cherniak, D.J., Watson, E.B., 2001. Pb diffusion in zircon. Chemical Geology 172, 5-24.

Chevalier, J., Gremillard, L., Virkar, A.V., Clarke, D.R., 2009. The Tetragonal-Monoclinic Transformation in Zirconia: Lessons Learned and Future Trends. Journal of the American Ceramic Society 92, 1901-1920.

Day, J.M., Moynier, F., 2014. Evaporative fractionation of volatile stable isotopes and their bearing on the origin of the Moon. Philosophical Transactions of the Royal Society of London A: Mathematical, Physical and Engineering Sciences 372, 20130259.

Drake, M.J., Righter, K., 2002. Determining the composition of the Earth. Nature 416, 39-44.

Erickson, T.M., Pearce, M.A., Reddy, S.M., Timms, N.E., Cavosie, A.J., Bourdet, J., Rickard, W.D.A., Nemchin, A.A., 2017. Microstructural constraints on the mechanisms of the transformation to reidite in naturally shocked zircon. Contributions to Mineralogy and Petrology 172, 6.

Ferrière, L., Koeberl, C., Reimold, W.U., 2009. Characterisation of ballen quartz and cristobalite in impact breccias: new observations and constraints on ballen formation. European Journal of Mineralogy 21, 203-217.

French, B.M., Koeberl, C., 2010. The convincing identification of terrestrial meteorite impact structures: What works, what doesn't, and why. Earth-Science Reviews 98, 123-170.

Gibbons, R.V., Morris, R.V., Horz, F., Thompson, T.D., 1975. Petrographic and ferromagnetic resonance studies of experimentally shocked regolith analogs. Lunar and Planetary Science Conference Proceedings 6, 3143-3171.

Glass, B.P., Simonson, B.M., 2012. Distal Impact Ejecta Layers: Spherules and More. Elements 8, 43-48.

Gomes, R., Levison, H.F., Tsiganis, K., Morbidelli, A., 2005. Origin of the cataclysmic Late Heavy Bombardment period of the terrestrial planets. Nature 435, 466-469.

Grieve, R.A., Dence, M.R., Robertson, P.B., 1977. Cratering processes-As interpreted from the occurrence of impact melts., in: Roddy, D.J., Pepin, R.O., Merrill, R.B. (Eds.), Impact and explosion cratering: Planetary and terrestrial implications; Proceedings of the Symposium on Planetary Cratering Mechanics, Flagstaff, Ariz., September 13-17, 1976. Symposium sponsored by the Lunar and Planetary Institute New York, Pergamon Press, Inc., 1977, New York, pp. 791-814.

Hart, S.R., Davis, K.E., 1978. Nickel partitioning between olivine and silicate melt. Earth and Planetary Science Letters 40, 203-219.

Heisinger, H., Head, J.W., 2006. New views of lunar geoscience: An introduction and overview, in: Jolliff, B.L., Wieczorek, M.A., Shearer, C.K., Neal, C.R. (Eds.), New Views of the Moon. Reviews in Mineralogy and Geochemistry, pp. 1-81.

Heuer, A.H., Chaim, R., & Lanteri, V., 1987. The displacive cubic→ tetragonal transformation in ZrO_2 alloys. Acta Metallurgica 35, 661-666.

Hörz, F., Cintala, M.J., See, T.H., Le, L., 2005. Shock melting of ordinary chondrite powders and implications for asteroidal regoliths. Meteoritics & Planetary Science 40, 1329-1346.

Kaiser, A., Lobert, M., Telle, R., 2008. Thermal stability of zircon ($ZrSiO_4$). Journal of the European Ceramic Society 28, 2199-2211.

Keays, R.R., Lightfoot, P.C., 2004. Formation of Ni-Cu-Platinum Group Element sulfide mineralization in the Sudbury Impact Melt Sheet. Mineralogy and Petrology 82, 217-258.

Kerschhofer, L., Schärer, U., Deutsch, A., 2000. Evidence for crystals from the lower mantle: baddeleyite megacrysts of the Mbuji Mayi kimberlite. Earth and Planetary Science Letters 179, 219-225.

Kieffer, S.W., Phakey, P.P., Christie, J.M., 1976. Shock processes in porous quartzite: Transmission electron microscope observations and theory. Contributions to Mineralogy and Petrology 59, 41-93.

Korhonen, F.J., Clark, C., Brown, M., Taylor, R.J.M., 2014. Taking the temperature of Earth's hottest crust. Earth and Planetary Science Letters 408, 341-354.

Kring, D.A., Cohen, B.A., 2002. Cataclysmic bombardment throughout the inner solar system 3.9–4.0 Ga. Journal of Geophysical Research: Planets 107.

Kubaschewski, O., 1982. Iron—Binary phase diagrams. Springer-Verlag, Berlin Heidelberg.

Kyte, F.T., Bohor, B.F., 1995. Nickel-rich magnesiowüstite in Cretaceous/Tertiary boundary spherules crystallized from ultramafic, refractory silicate liquids. Geochimica et Cosmochimica Acta 59, 4967-4974.

Lamoreaux, R.H., Hildenbrand, D.L., Brewer, L., 1987. High‐Temperature Vaporization Behavior of Oxides II. Oxides of Be, Mg, Ca, Sr, Ba, B, Al, Ga, In, Tl, Si, Ge, Sn, Pb, Zn, Cd, and Hg. Journal of Physical and Chemical Reference Data 16, 419-443.

Lindsley, D.H., Andersen, D.J., 1983. A two-pyroxene thermometer. Journal of Geophysical Research 88, A887.

Lou, V.L.K., Mitchell, T.E., Heuer, A.H., 1985. REVIEW─Graphical Displays of the Thermodynamics of High‐Temperature Gas‐Solid Reactions and Their Application to Oxidation of Metals and Evaporation of Oxides. Journal of the American Ceramic Society 68, 49-58.

Marchi, S., Black, B.A., Elkins-Tanton, L.T., Bottke, W.F., 2016. Massive impact-induced release of carbon and sulfur gases in the early Earth's atmosphere. Earth and Planetary Science Letters 449, 96-104.

Marchi, S., Bottke, W.F., Elkins-Tanton, L.T., Bierhaus, M., Wuennemann, K., Morbidelli, A., Kring, D.A., 2014. Widespread mixing and burial of Earth's Hadean crust by asteroid impacts. Nature 511, 578-582.

Marchi, S., Chapman, C.R., Fassett, C.I., Head, J.W., Bottke, W.F., Strom, R.G., 2013. Global resurfacing of Mercury 4.0-4.1 billion years ago by heavy bombardment and volcanism. Nature 499, 59-61.

Marion, C.L., Sylvester, P.J., 2010. Composition and heterogeneity of anorthositic impact melt at Mistastin Lake crater, Labrador. Planetary and Space Science 58, 552-573.

Melosh, H.J., 1989. Impact cratering: A geologic process. Research supported by NASA. Oxford University Press, New York.

Melosh, H.J., 2005. The mechanics of pseudotachylite formation in impact events, in: Koeberl, C., Henkel, H. (Eds.), Impact tectonics. Springer, Berlin Heidelberg, pp. 55-80.

Melosh, H.J., 2008. Did an impact blast away half of the martian crust? Nature Geoscience 1, 412-414.

Monteux, J., Amit, H., Choblet, G., Langlais, B., Tobie, G., 2015. Giant impacts, heterogeneous mantle heating and a past hemispheric dynamo on Mars. Physics of the Earth and Planetary Interiors 240, 114-124.

Morbidelli, A., Marchi, S., Bottke, W.F., Kring, D.A., 2012. A sawtooth-like timeline for the first billion years of lunar bombardment. Earth and Planetary Science Letters 355, 144-151.

Moynier, F., Beck, P., Yin, Q.Z., Ferroir, T., Barrat, J.A., Paniello, R., Telouk, P., Gillet, P., 2010. Volatilization induced by impacts recorded in Zn isotope composition of ureilites. Chemical Geology 276, 374-379.

Onorato, P.I.K., Uhlmann, D.R., Simonds, C.H., 1978. The thermal history of the Manicouagan impact melt sheet, Quebec. Journal of Geophysical Research: Solid Earth 83, 2789-2798.

Pearce, M.A., Timms, N.E., Hough, R.M., Cleverley, J.S., 2013. Reaction mechanism for the replacement of calcite by dolomite and siderite: implications for geochemistry, microstructure and porosity evolution during hydrothermal mineralisation. Contributions to Mineralogy and Petrology 166, 995-1009.

Pringle, E.A., Moynier, F., Savage, P.S., Badro, J., Barrat, J.A., 2014. Silicon isotopes in angrites and volatile loss in planetesimals. Proceedings of the National Academy of Sciences 111, 17029-17032.

Riller, U., Lieger, D., Gibson, R.L., Grieve, R.A., Stöffler, D., 2010. Origin of large-volume pseudotachylite in terrestrial impact structures. Geology 38, 619-622.

Ryder, G., 2002. Mass flux in the ancient Earth‐Moon system and benign implications for the origin of life on Earth. Journal of Geophysical Research: Planets 107.

Sack, R.O., Ghiorso, M.S., 1991. Chromian spinels as petrogenetic indicators; thermodynamics and petrological applications. American Mineralogist 76, 827-847.

Simonds, C.H., 1975. Thermal regimes in impact melts and the petrology of the Apollo 17 Station 6 boulder. Lunar and Planetary Science Conference Proceedings 6, 641-672.

Sleep, N.H., 2016. Asteroid bombardment and the core of Theia as possible sources for the Earth's late veneer component. Geochemistry, Geophysics, Geosystems 17, 2623-2642.

Spray, J.G., 1998. Localized shock-and friction-induced melting in response to hypervelocity impact. Geological Society, London, Special Publications 140, 195-204.

Stöffler, D., 1971. Deformation and transformation of rock-forming minerals by natural and experimental shock processes. I - Behavior of minerals under shock compression. Fortschritte der Mineralogie 49, 50-113.

Swab, J., 2001. Role of oxide additives in stabilizing zirconia for coating applications. Army Research Laboratory, Aberdeen Proving Ground.

Swamy, V., Saxena, S.K., Sundman, B., Zhang, J., 1994. A thermodynamic assessment of silica phase diagram. Journal of Geophysical Research: Solid Earth 99, 11787-11794.

Sylvester, P., Crowley, J., Schmitz, M., 2013. U–Pb zircon age of Mistastin Lake crater, Labrador, Canada–implications for high-precision dating of small impact melt sheets and the end Eocene extinction, Goldschmidt. Mineralogical Magazine, Florence, Italy, p. 2295.

Taylor, R.J.M., Harley, S.L., Hinton, R.W., Elphick, S., Clark, C., Kelly, N.M., 2015. Experimental determination of REE partition coefficients between zircon, garnet and melt: a key to understanding high-Tcrustal processes. Journal of Metamorphic Geology 33, 231-248.

Timms, N.E., Erickson, T.M., Pearce, M.A., Cavosie, A.J., Schmieder, M., Tohver, E., Reddy, S.M., Zanetti, M., Nemchin, A.A., Wittmann, A., 2017. A pressure-temperature phase diagram for zircon at extreme conditions. Earth Science Reviews 165, 185-202.

Timms, N.E., Reddy, S.M., Healy, D., Nemchin, A.A., Grange, M.L., Pidgeon, R.T., Hart, R., 2012. Resolution of impact-related microstructures in lunar zircon: A shock-deformation mechanism map. Meteoritics & Planetary Science 47, 120-141.

Tschauner, O., Ma, C., Beckett, J.R., Prescher, C., Prakapenka, V.B., Rossman, G.R., 2014. Discovery of bridgmanite, the most abundant mineral in Earth, in a shocked meteorite. Science 346.

Watters, W.A., Zuber, M.T., Hager, B.H., 2009. Thermal perturbations caused by large impacts and consequences for mantle convection. Journal of Geophysical Research 114.

Wünnemann, K., Collins, G.S., Osinski, G.R., 2008. Numerical modelling of impact melt production in porous rocks. Earth and Planetary Science Letters 269, 530-539.

Zanetti, M.R., 2015. Investigating the Complexity of Impact Crater Ejecta, Department of Earth and Planetary Sciences. Washington University in St. Louis, St. Louis, Missouri, USA, p. 218.

Graphical Abstract (for review)

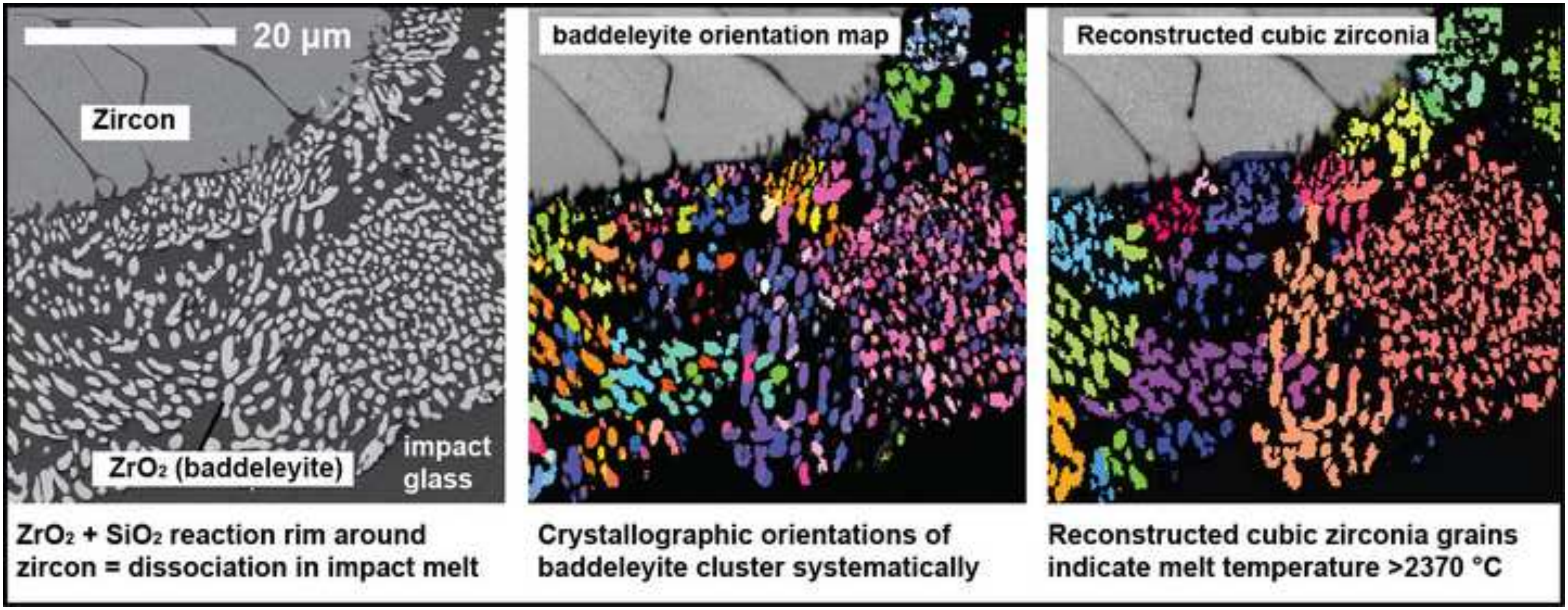

Figure 1

Click here to download high resolution image

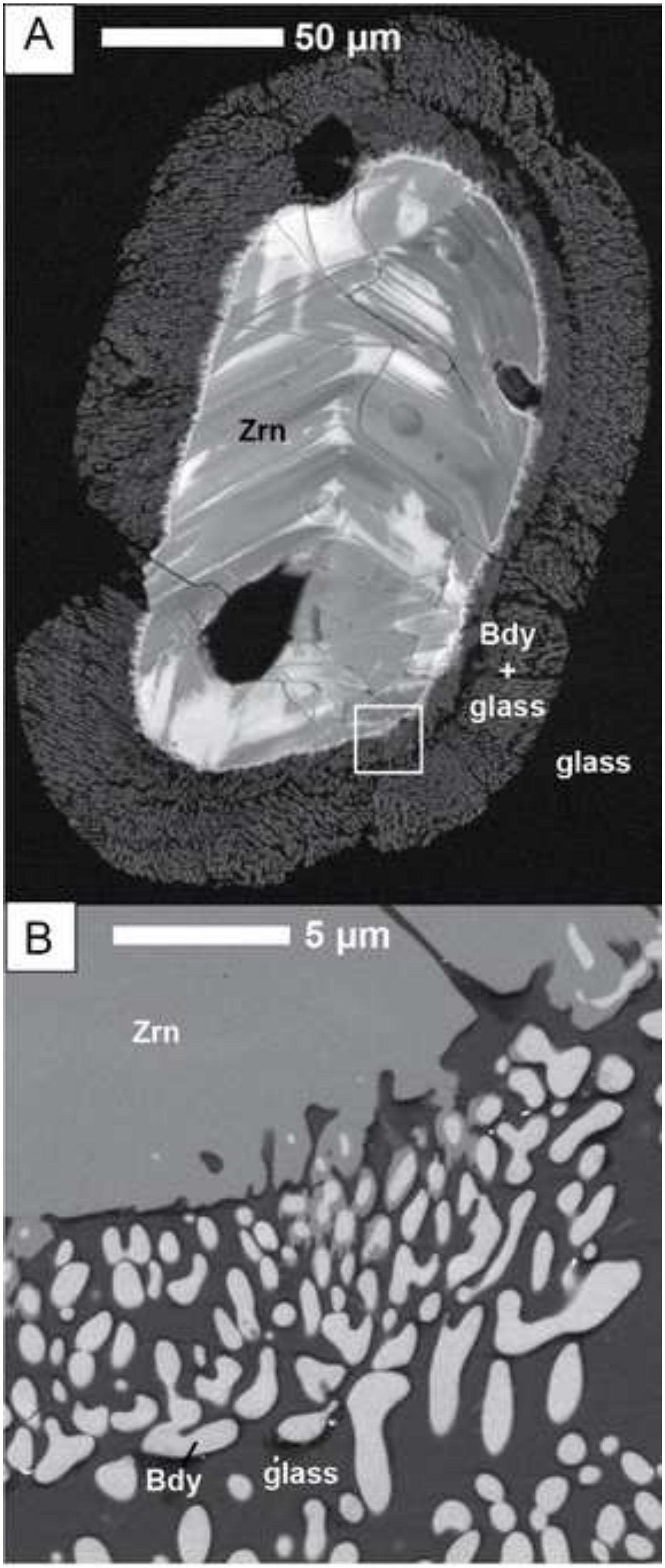

Timms et al. Figure 1

Figure 2

Click here to download high resolution image

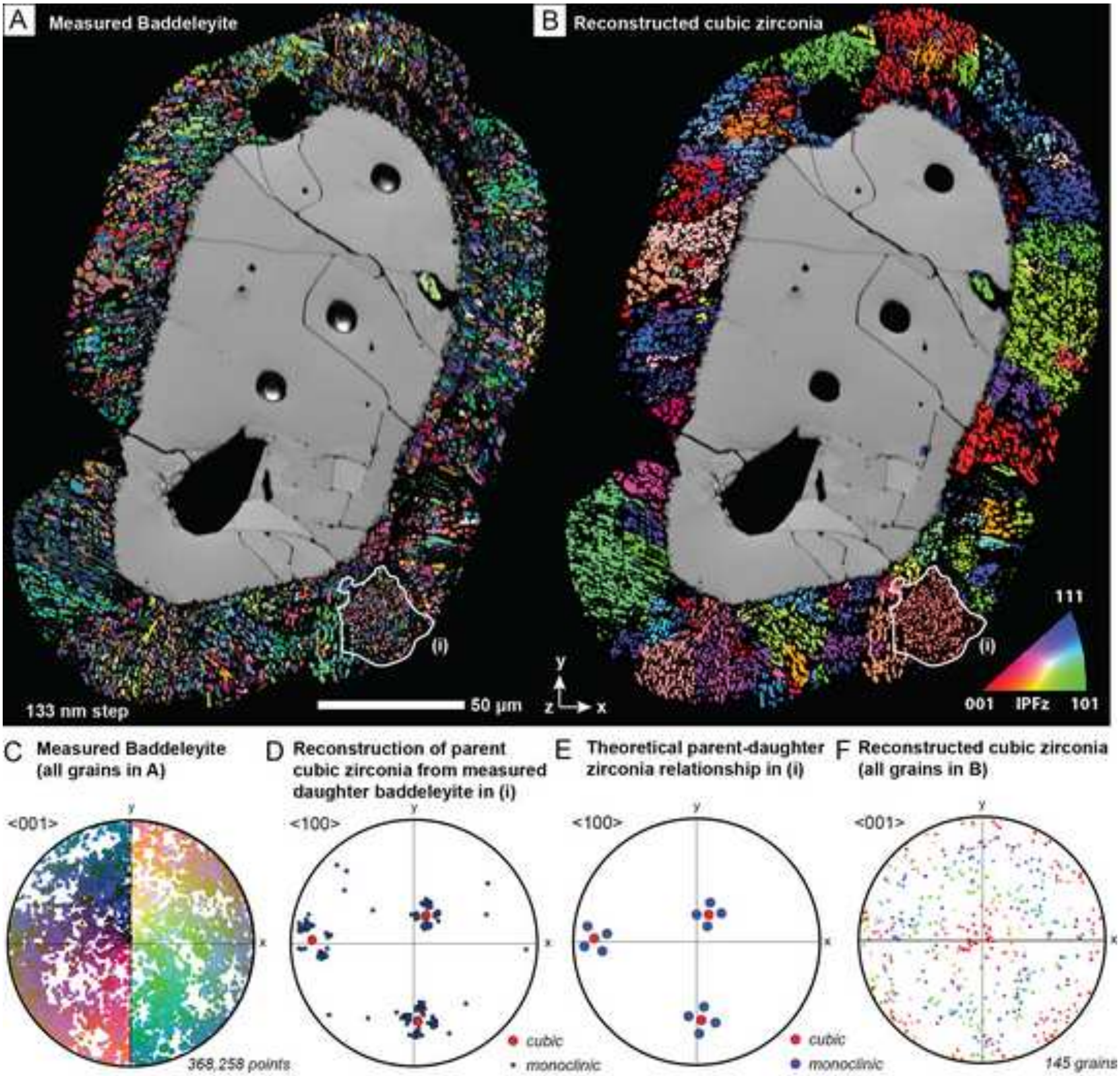

Timms et al. Figure 2

Figure 3
Click here to download high resolution image

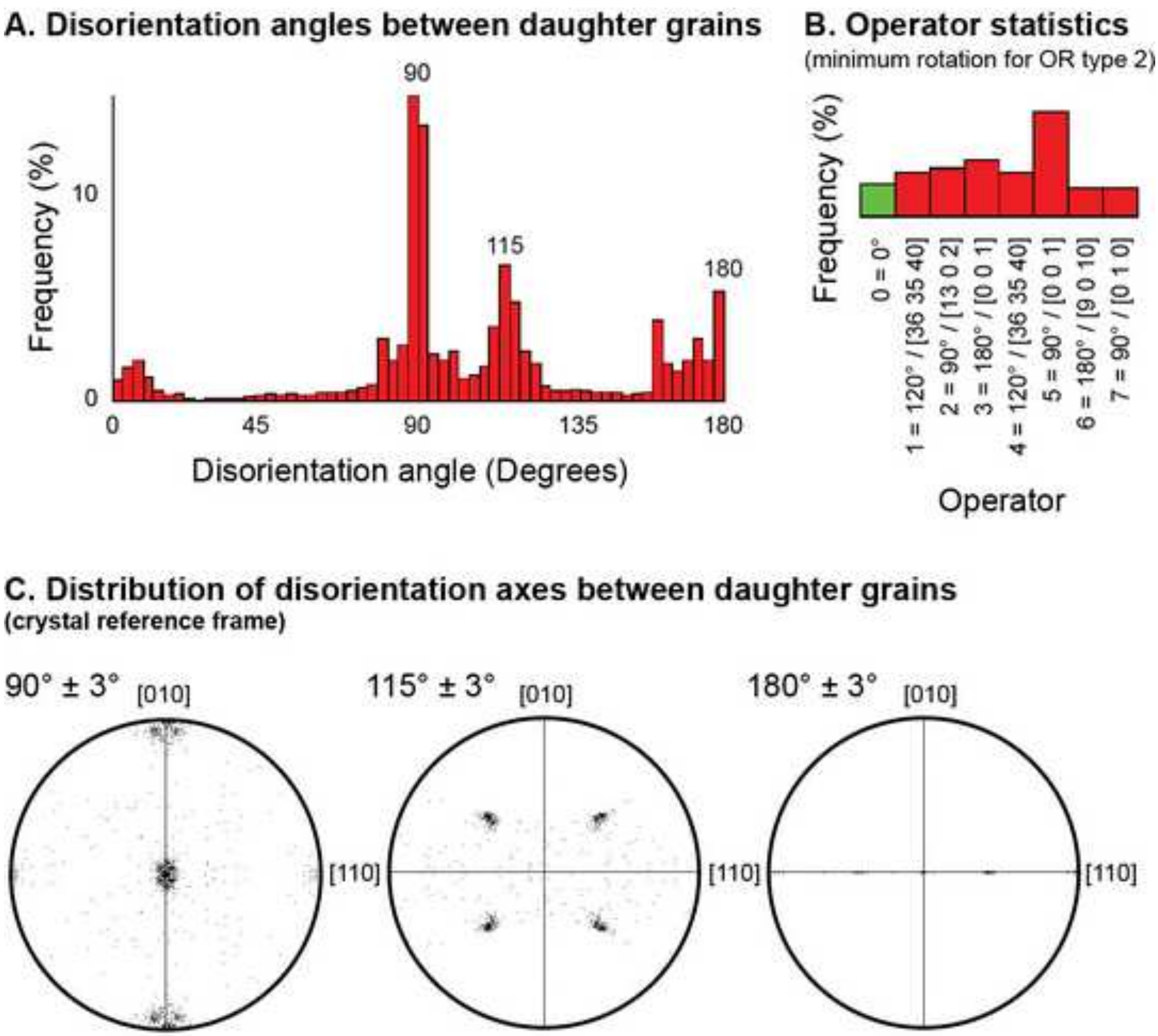

Timms et al. Figure 3

Figure 4
Click here to download high resolution image

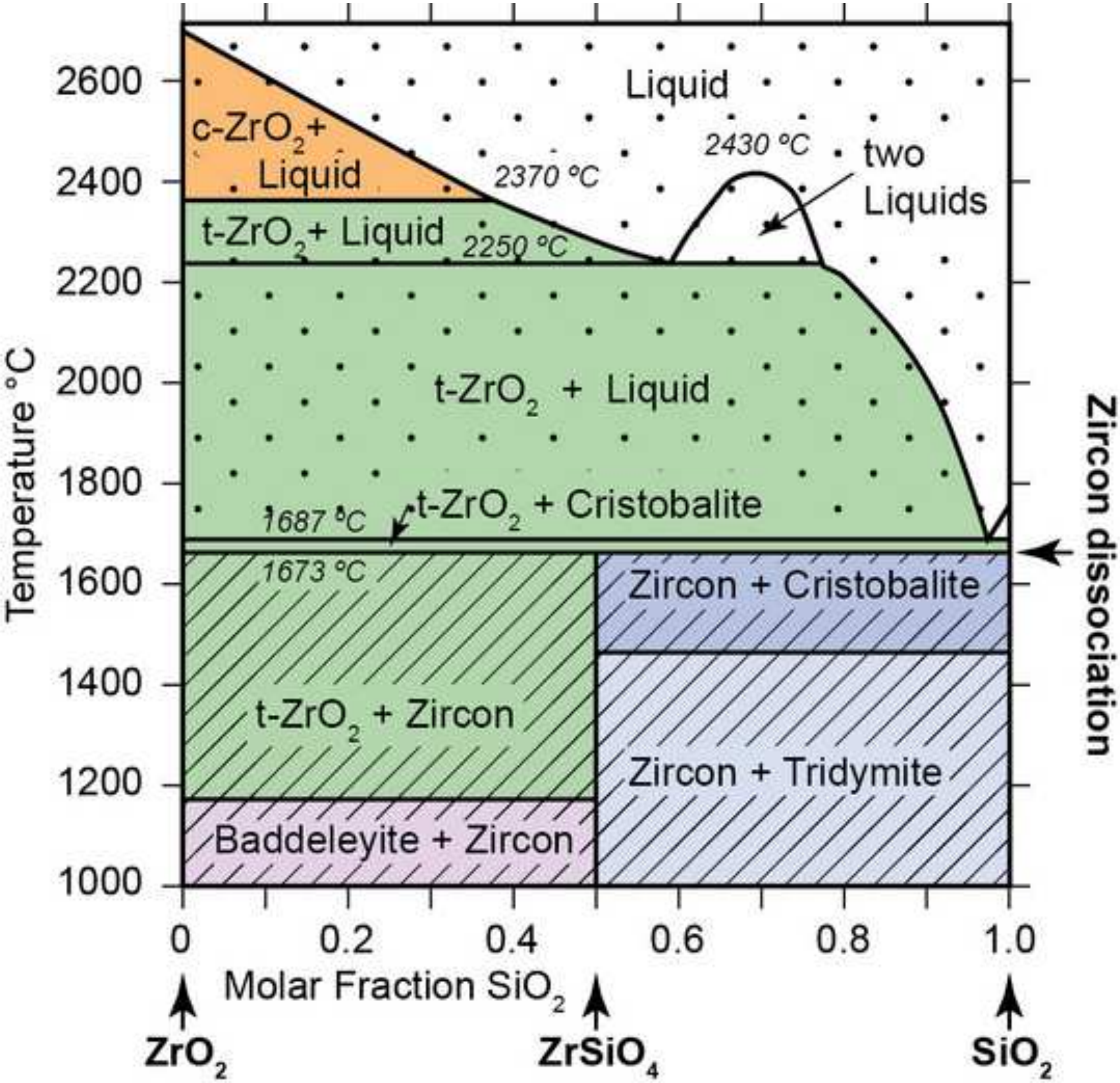

Timms et al. Figure 4

Figure 5

Click here to download high resolution image

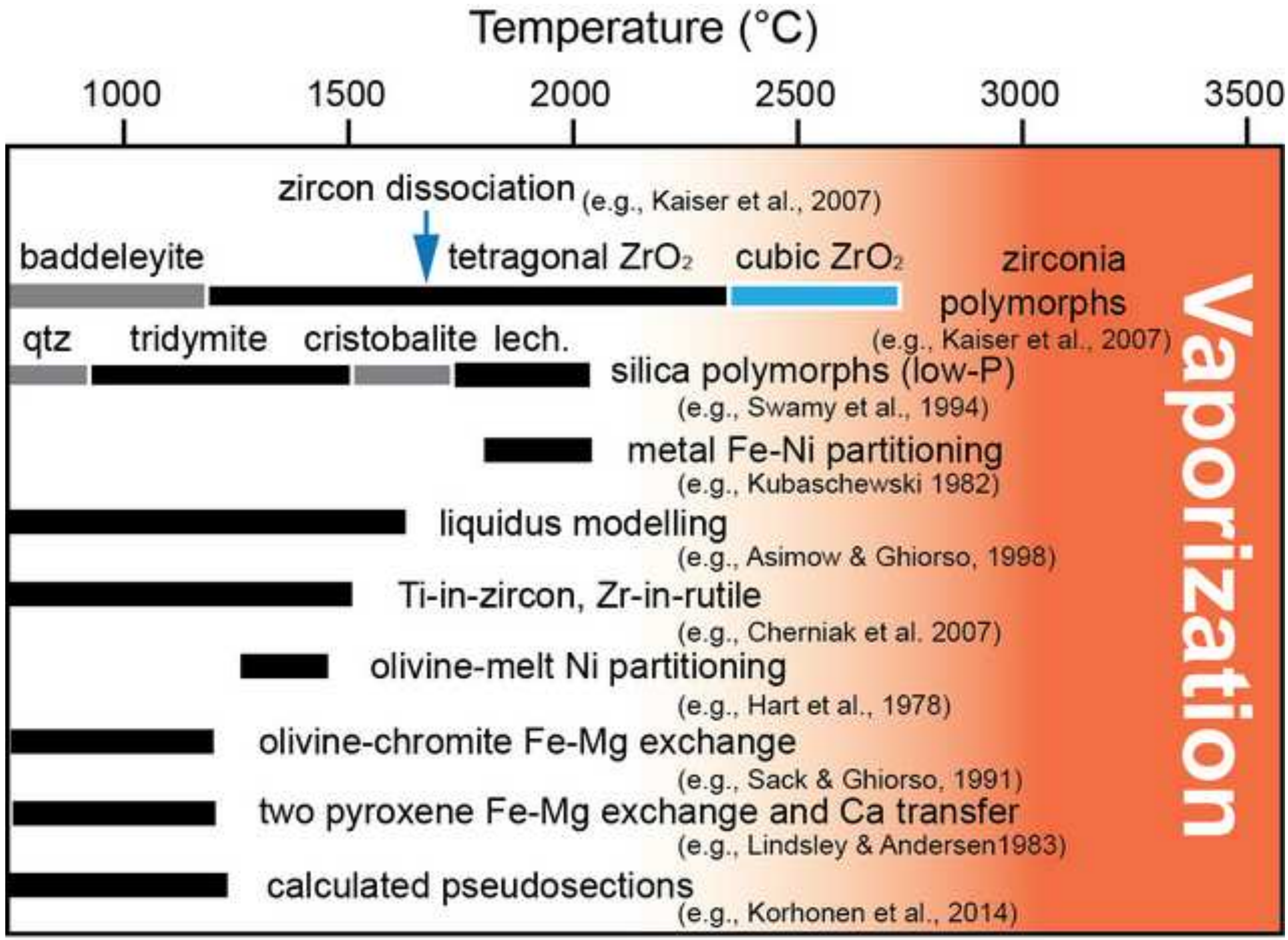

Timms et al. Figure 5

Supplementary File

Cubic zirconia in >2370 °C impact melt records Earth's hottest crust

Nicholas E. Timms[1]*, Timmons M. Erickson[1], Michael R. Zanetti[2], Mark A. Pearce[3], Cyril Cayron[4], Aaron J. Cavosie[1,5], Steven M. Reddy[1], Axel Wittmann[6], Paul K. Carpenter[7]

[1] Department of Applied Geology, Curtin University, Perth, GPO Box U1987, Western Australia 6845, Australia
[2] University of Western Ontario, 1151 Richmond St, London, Ontario, N6A 3K7, Canada
[3] CSIRO Mineral Resources, Australian Resources Research Centre, 26 Dick Perry Avenue, Kensington, WA 6151, Australia
[4] Laboratory of ThermoMechanical Metallurgy (LMTM), PX Group Chair, École Polytechnique Fédérale de Lausanne (EPFL), Rue de la Maladière 71b, 2000 Neuchâtel, Switzerland
[5] NASA Astrobiology Institute, Department of Geoscience, University of Wisconsin-Madison, Madison WI, USA
[6] LeRoy Eyring Center for Solid State Science, Arizona State University, 901 S Palm Walk, Tempe, AZ, 85287, USA
[7] Washington University in St Louis, Earth and Planetary Science Department and the McDonnell Center for Space Sciences; 1 Brookings Drive, St Louis MO, 63112, USA

*Corresponding author email: n.timms@curtin.edu.au

Contents

Item 1. Sample preparation and scanning electron microscopy (SEM) data collection methods and settings
Item 2. Summary of images and electron backscatter diffraction (EBSD) data from MZRN-1
Item 3. Summary of images and electron backscatter diffraction (EBSD) data from MZRN-2
Item 4. Electron microprobe microanalysis (EPMA) methods and settings
Item 5. Reconstruction of parent cubic zirconia grains from daughter monoclinic zirconia crystallographic orientation data
Item 6. Transformation twin relationships in the baddeleyite corona
Item 7. Effects of impurities and pressure on zirconia polymorph stability
Item 8. Supplemental Reference List

Item 1. Sample preparation and scanning electron microscopy (SEM) data collection methods and settings

Sample preparation

We polished the petrographic sections of the sample with 1 μm diamond paste prior to mounting regions of interest that include the zircon grains into an epoxy disk. The sample was given a further chemical-mechanical polish for EBSD analysis using colloidal silica in NaOH for three hours on a Buehler Vibromet II polisher. A thin coat of carbon was applied to mitigate charging during electron microscopy yet permit EBSD patterns to be acquired.

Cathodoluminescence and backscatter electron imaging

At Curtin University, we performed scanning electron microscopy (SEM) using a Tescan MIRA3 field emission (FE-)SEM and atomic number contrast imaging with a pole piece backscatter detector, an accelerating voltage of 5 kV, a beam current of 22 nA, and a working distance of 15 mm. Moreover, we did cathodoluminescence imaging at 15 kV acceleration voltage and 15 mm working distance.

Electron backscatter diffraction (EBSD) mapping

We did orientation mapping via EBSD, using a Tescan MIRA3 FE-SEM with an Oxford Instruments AZTEC EDS/EBSD acquisition system at Curtin University. Operation conditions were optimised for EBSD and include a stage tilt of 70° around a horizontal axis and beam acceleration voltage of 20 kV (Prior et al., 1999). We processed EBSD patterns using 4 x 4 pixel binning and indexed using match units for zircon, cubic, orthorhombic, tetragonal and monoclinic ZrO_2 (Table S1). However, only zircon and baddeleyite could be indexed. The mean 'mean angular deviation' for zircon and baddeleyite indexing solutions was 0.41° and 0.50°, respectively.

We processed the EBSD data using Oxford Instruments Channel 5.12 software. Maps were noise reduced by removing isolated erroneous data points ('wildspike' correction) followed by a zero solution extrapolation to six nearest neighbours. Visual inspection shows that no significant artefacts were generated during noise reduction. We generated thematic maps using the Tango module of Channel 5, and include phase, EBSD pattern quality (band contrast), and crystallographic orientation maps (Figs S1 and S2). Pole figures were generated using the Mambo module of Channel 5 (Figs S1 and S2).

Table S1. Scanning electron microscopy settings and electron backscatter diffraction analysis acquisition and processing parameters.

SEM		
Make/model	Tescan Mira3 FEG-SEM	
EBSD acquisition system	Oxford Instruments Aztec / Nordlys EBSD Detector	
EBSD Processing software	Oxford Instruments Channel 5.10	
Acceleration Voltage (kV)	20	
Working Distance (mm)	~20.5	
Tilt	70°	
EBSD match units		
Zircon	Zircon5260, 1 atm (Hazen and Finger, 1979)	
Reidite	Reidite632, 0.69 GPa (Farnan et al., 2003)	
Baddeleyite (monoclinic ZrO_2)	(Bondars et al., 1995), (Hill and Cranswick, 1994)	
Tetragonal ZrO_2	(Teufer, 1962)	
Cubic ZrO_2	ICSD card 53998 (Böhm, 1925)	
Orthorhombic ZrO_2	ICSD card 77716	
Quartz	'Quartznew', HKL database (Sands, 1969)	
Cristobalite	(Downs and Palmer, 1994)	
Coesite	(Kirfe et al., 1979)	
EBSP Acquisition, Indexing and Processing		
Sample Location	**Discovery Hill, Mistastin Lake, Canada**	
Grain ID	MZRN-1	MZRN-2
Figures	2, S1, S3, S5	S2, S4, S6, S7
EBSP Acquisition Speed (Hz)	40	40
EBSP Background (frames)	64	64
EBSP Binning	4 x 4	4 x 4
EBSP Gain	High	High
Hough resolution	60	60
Band detection (min / max)	6 / 8	6 / 8
Mean angular deviation (zircon)	<1°	<1°
Mean angular deviation (reidite)	n/a	n/a
Mean angular deviation (baddeleyite)	<1°	<1°
Map step size (nm)	133	80
Map size (X steps / Y steps)	1428 / 1862	1495 / 1435
EBSD noise reduction routine		
Wildspike correction	Yes	Yes
Nearest neighbour zero solution extrapolation	6	6

Item 2. Summary of images and electron backscatter diffraction (EBSD) data from MZRN-1

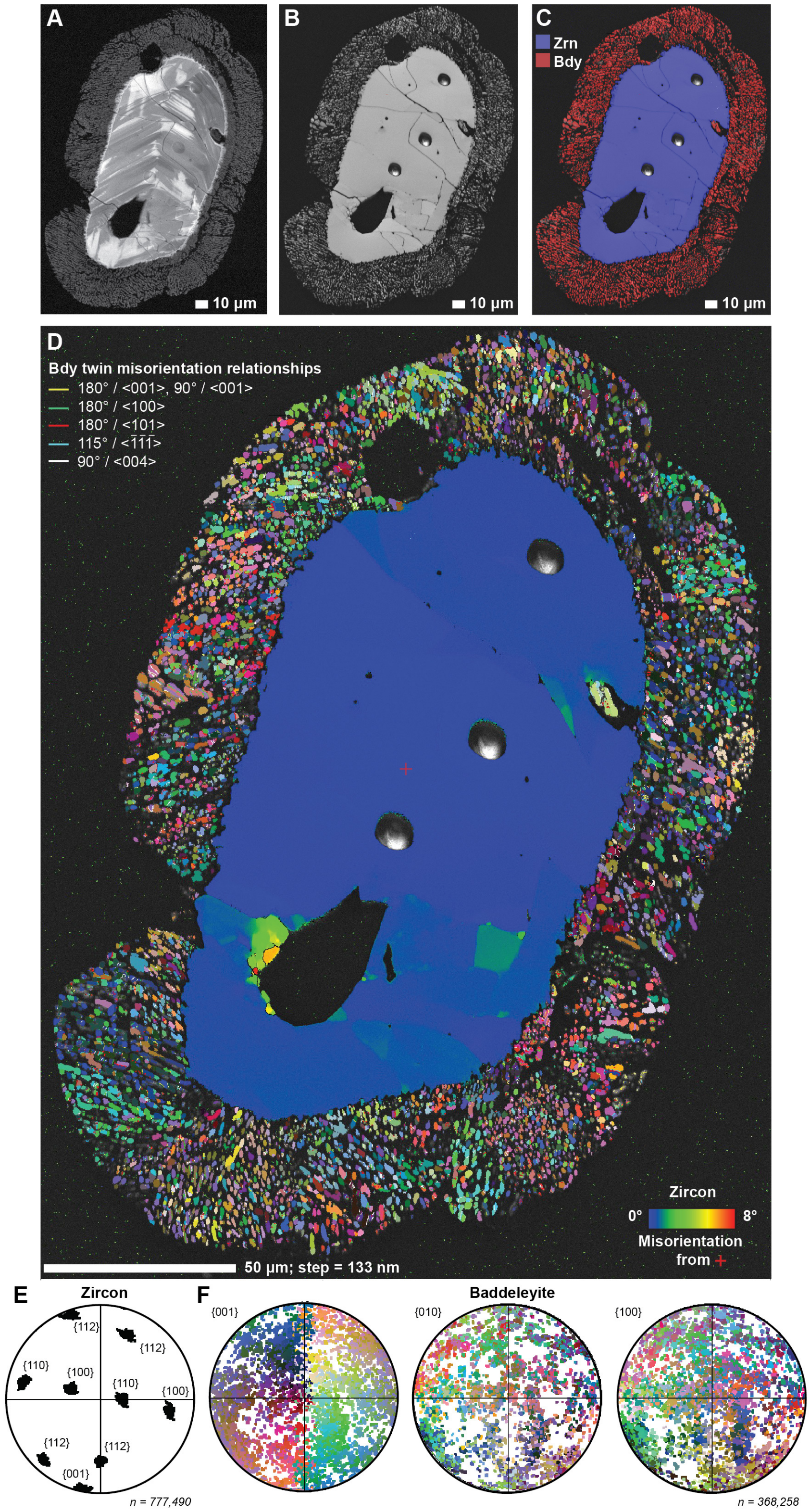

Figure S1. MZRN-1 A. CL image. B. EBSD pattern quality (band contrast) map. C. Phase map from EBSD data. D. EBSD map showing ~8° cumulative misorientations recorded by MZRN-1, solely attributed to brittle fracture block rotation. No crystal-plastic microstructures, twinning or reidite were detected. Baddeleyite in corona coloured for orientation using All Euler scheme. E. Pole figure of principal planes of zircon. F. Pole figures of principal planes of baddeleyite. E and F are lower hemisphere equal area projections in the map x-y-z reference frame.

Item 3. Summary of images and electron backscatter diffraction (EBSD) data from MZRN-2

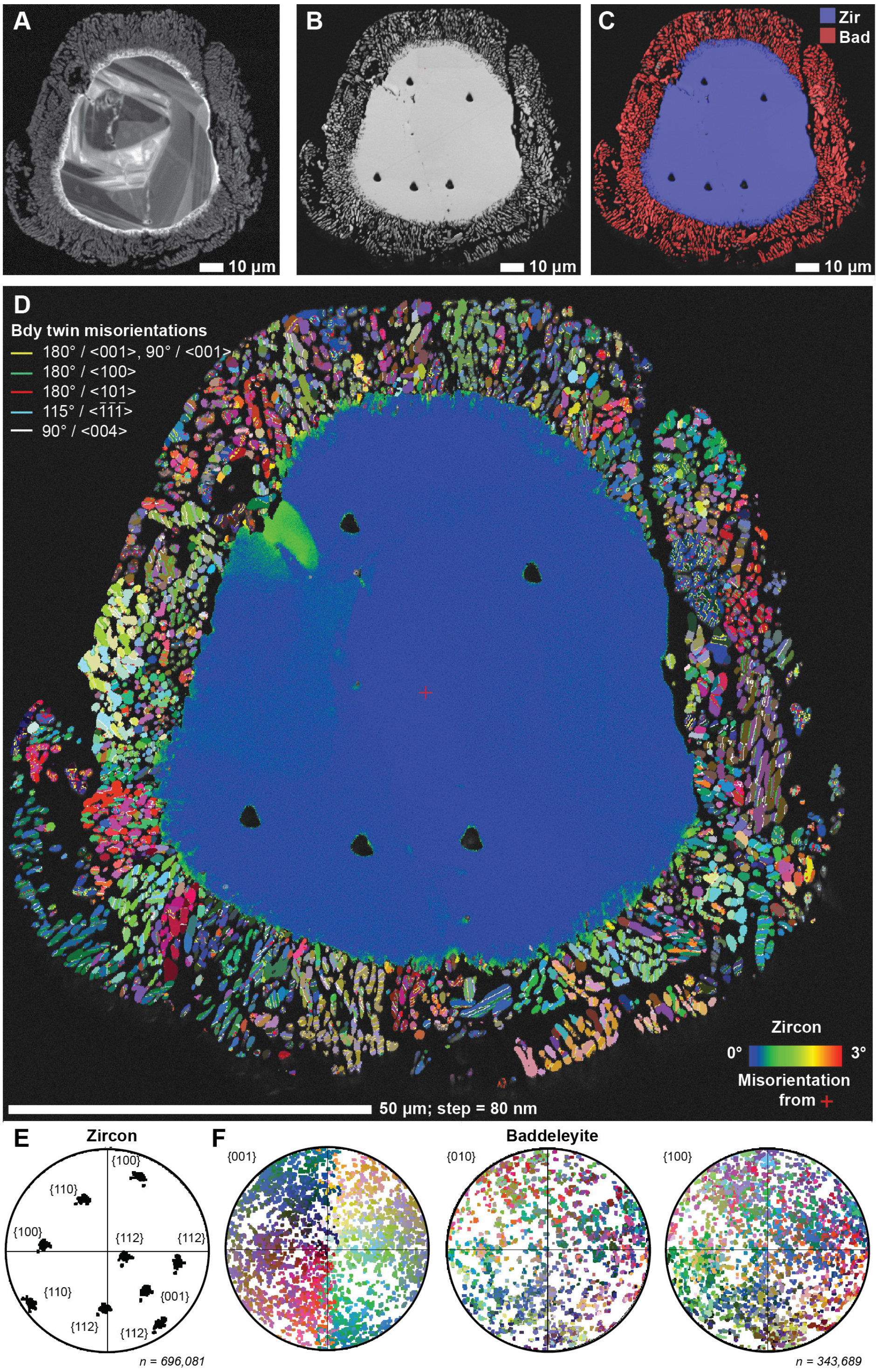

Figure S2. MZRN-2 A. CL image. B. EBSD pattern quality (band contrast) map. C. Phase map from EBSD data. D. EBSD map showing <3° cumulative misorientation recorded by MZRN-2, solely attributed to brittle fracture block rotation. A minor amount of crystal-plastic strain is preserved near the dissociation interface. No other crystal-plastic microstructures, twinning or reidite indicative of shock metamorphism were detected. Baddeleyite in corona coloured for orientation using All Euler scheme. E. Pole figure of principal planes of zircon. F. Pole figures of principal planes of baddeleyite. E and F are lower hemisphere equal area projections in the map x-y-z reference frame.

Item 4. Electron microprobe microanalysis (EPMA) methods and settings

We measured the concentration of selected trace elements of zircon and zirconia using a JEOL JXA-8200 electron probe microanalyser at the Department of Earth and Planetary Sciences of Washington University in St Louis, USA. This instrument is equipped with 5 wavelength-dispersive spectrometers, and an e2v silicon-drift energy-dispersive X-ray spectrometer. The WDS spot analyses included Ca, Fe, P, Zr, Si, Hf, Ti, Dy, Er, Th, Y. We used a time-dependent intensity correction routine for the WDS analyses to quantify element concentrations using the Probe for EPMA software package (Table S2).

Table S2. Selected major and trace element concentrations in zirconia, zircon and impact melt glass from time dependent intensity WDS analysis, after Zanetti (2015). Concentrations in parts per million (ppm). Bdl = below detection limit.

Acc. V (kV)				
Probe current (nA)	150	150	50	50
Element	**Zircon core (bright CL)**	**Zircon core (dark CL)**	**Zircon rim**	**Baddeleyite**
Fe	250-475	360-800	840-1000	~300
Ti	150-250	170-330	200-400	~350
Th	~35	200-340	20?	~275
Y	Bdl	1000-1780	670	~90
Dy	Bdl	60?	10-220	Bdl
Er	Bdl	Bdl	≤ 150	Bdl
P	280	300-400	-	~640

Item 5. Reconstruction of parent cubic zirconia grains from daughter monoclinic zirconia crystallographic orientation data

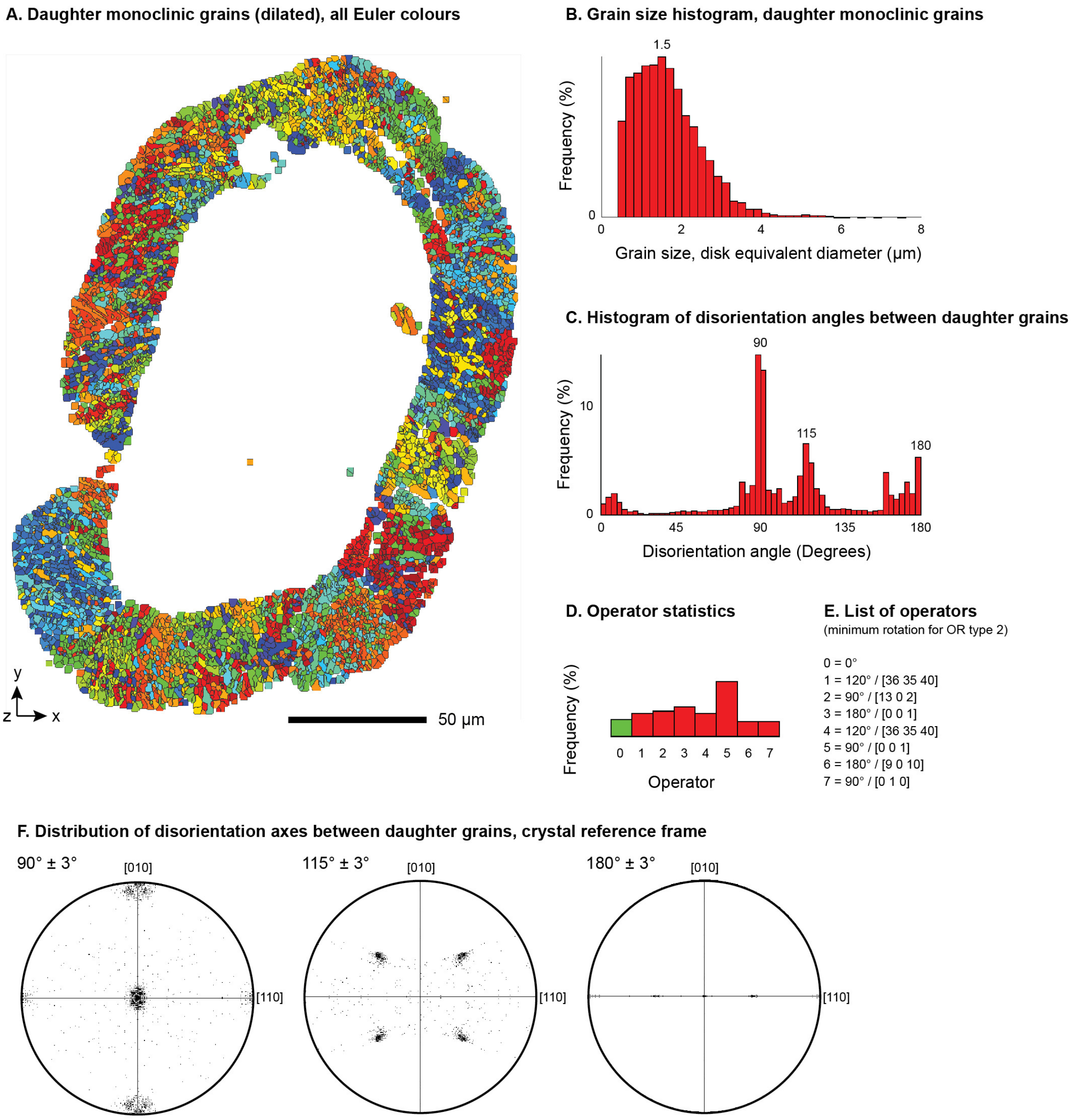

Figure S3. Results from orientation analysis of daughter monoclinic zirconia grains of MZRN-1 using the software ARPGE (Cayron, 2007; Cayron et al., 2010). A. Map showing the daughter monoclinic grains after grain the dilation procedure. All Euler colours represent different crystallographic orientations. B. Grain size histogram of daughter monoclinic grains shown in A. C. Histogram of disorientation angles between daughter monoclinic grains shown in A. D. Disorientation symmetry operator statistics for adjacent grains in A. E. List of disorientation operators for the type 2 orientation relationship (OR) of Cayron et al. (2010). F. Pole figures showing the distribution of 90°, 115°, and 180° disorientation axes between daughter grains in the crystal reference frame.

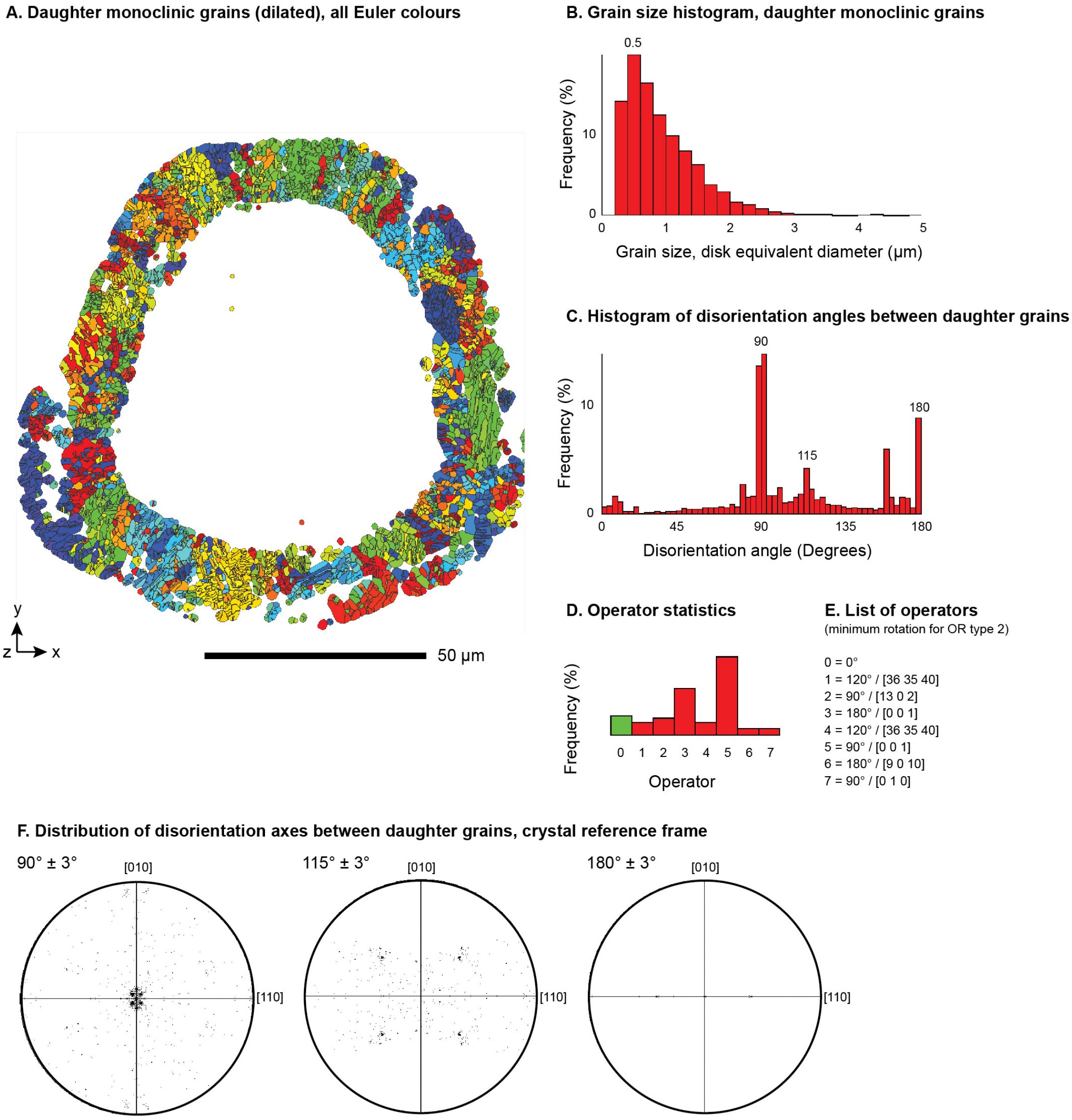

Figure S4. Results from orientation analysis of daughter monoclinic zirconia grains of MZRN-2 using the software ARPGE (Cayron, 2007; Cayron et al., 2010). A. Map showing the daughter monoclinic grains after grain the dilation procedure. All Euler colours represent different crystallographic orientations. B. Grain size histogram of daughter monoclinic grains shown in A. C. Histogram of disorientation angles between daughter monoclinic grains shown in A. D. Disorientation symmetry operator statistics for adjacent grains in A. E. List of disorientation operators for the type 2 orientation relationship (OR) of Cayron et al. (2010). F. Pole figures showing the distribution of 90°, 115°, and 180° disorientation axes between daughter grains in the crystal reference frame.

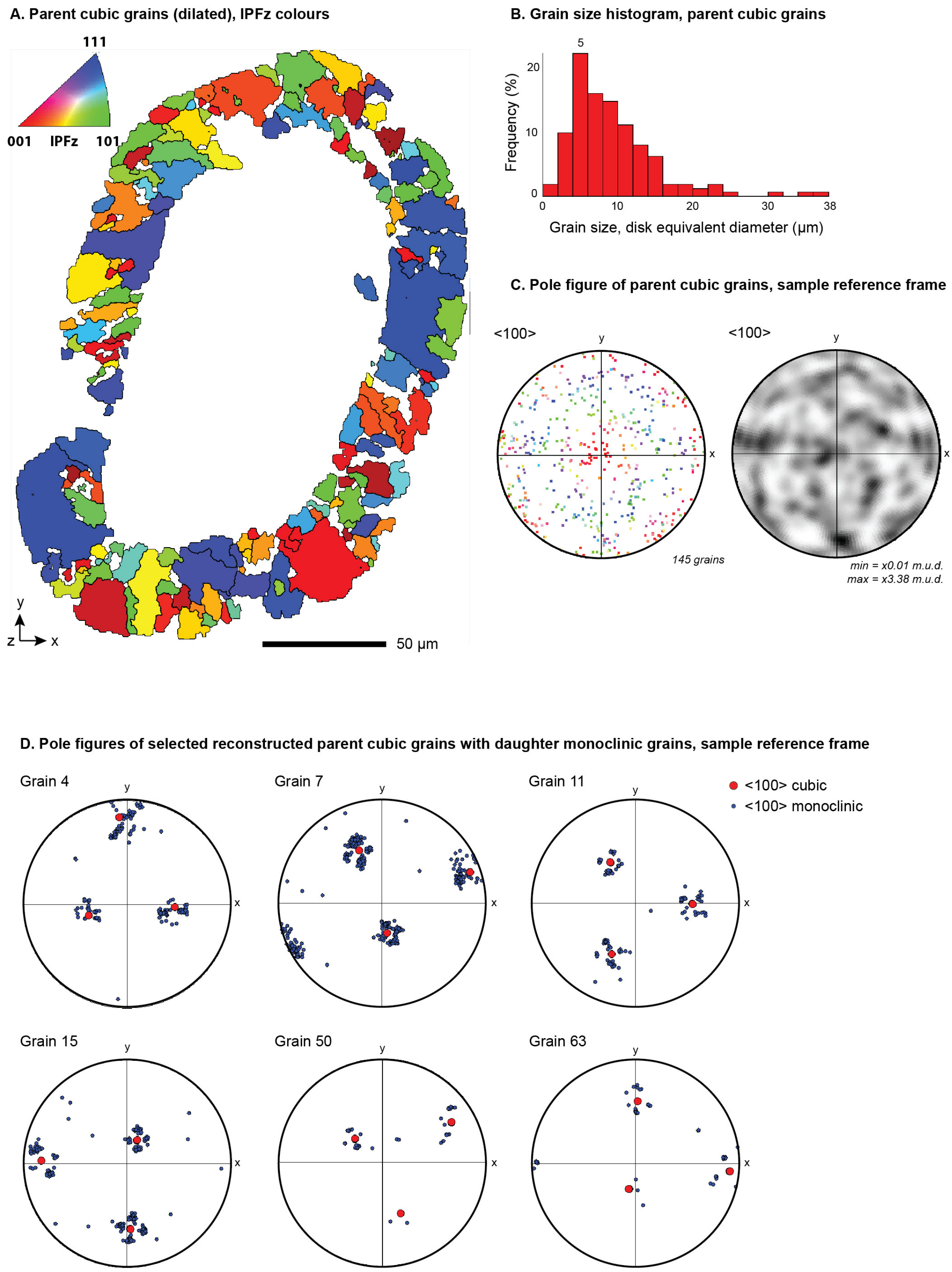

Figure S5. Reconstructed dilated parent cubic zirconia grains for MZRN-1 via the ARPGE software using type 2 OR after Cayron et al. (2010) (see Fig. S3). A. Map of parent cubic zirconia grains, all Euler orientation colour scheme. B. B. Grain size histogram of daughter monoclinic grains shown in A. C. Pole figure of <100> of the reconstructed cubic zirconia grains in the sample x-y-z reference frame. Left: colour scheme as in A; right: contoured at one point per grain. D. <100> Pole figures of selected reconstructed parent cubic zirconia grains (red) with daughter monoclinic zirconia grains (blue). Pole figures are lower hemisphere equal area projections in the map x-y-z reference frame.

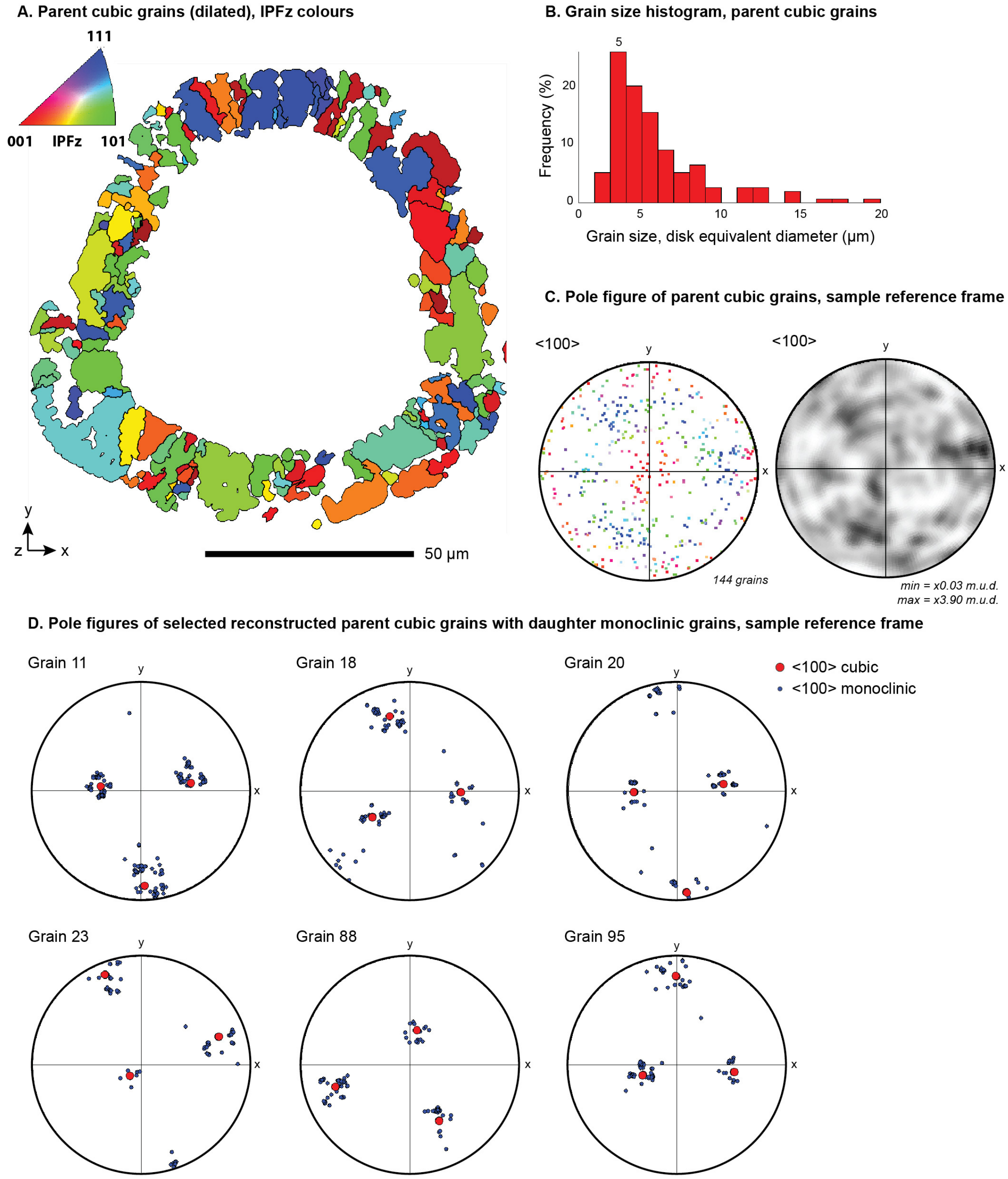

Figure S6. Reconstructed dilated parent cubic zirconia grains for MZRN-2 via the ARPGE software using type 2 OR after Cayron et al. (2010) (see Fig. S4). A. Map of parent cubic zirconia grains, all Euler orientation colour scheme. B. B. Grain size histogram of daughter monoclinic grains shown in A. C. Pole figure of <100> of the reconstructed cubic zirconia grains in the sample x-y-z reference frame. Left: colour scheme as in A; right: contoured at one point per grain. D. <100> Pole figures of selected reconstructed parent cubic zirconia grains (red) with daughter monoclinic zirconia grains (blue). Pole figures are lower hemisphere equal area projections in the map x-y-z reference frame.

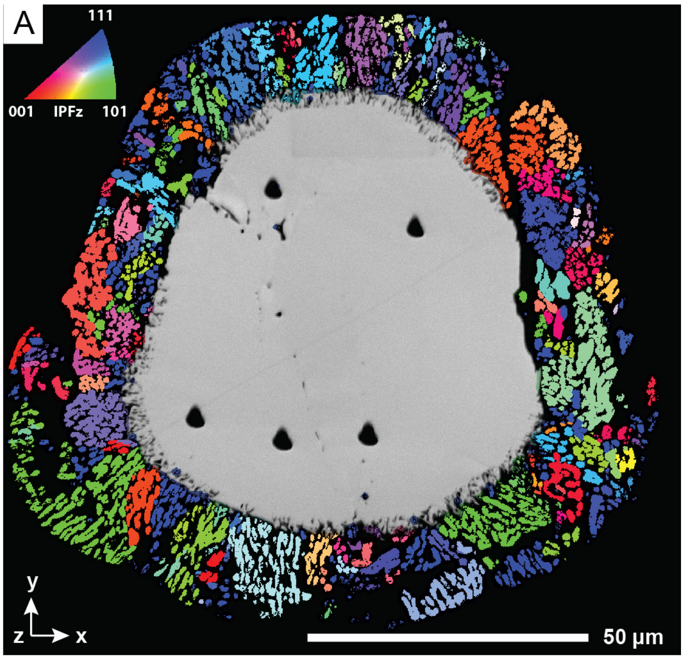

Figure S7. A. Map showing fully reconstructed parent cubic zirconia grains from MZRN-2. IPFz colour scheme. EBSD pattern quality (band contrast) for zircon shown in grayscale, and non-indexed points are black.

Item 6. Transformation twin relationships in the baddeleyite corona

Table S3. Transformation twin relationships in the baddeleyite corona. K_1 = composition plane; η_1 = shear direction.

Misorientation relationship	K_1	η_1	Type
180° <001>	(100)	[001]	Compound
180° <100>	(001)	[100]	Compound
180° <101>	$(\bar{1}0\bar{1})$	$[10\bar{1}]$	Compound
90° <004>		$[\bar{1}\bar{1}0]$	Type 2
90° <001>	$(1\bar{1}0)$		Type 1
90° <001>		$[0\bar{1}\bar{1}]$	Type 2
85° <100>	$(01\bar{1})$		Type 1
115° $< \bar{1}\bar{1}\bar{1} >$	?	?	unknown

Item 7. Effects of impurities and pressure on zirconia polymorph stability

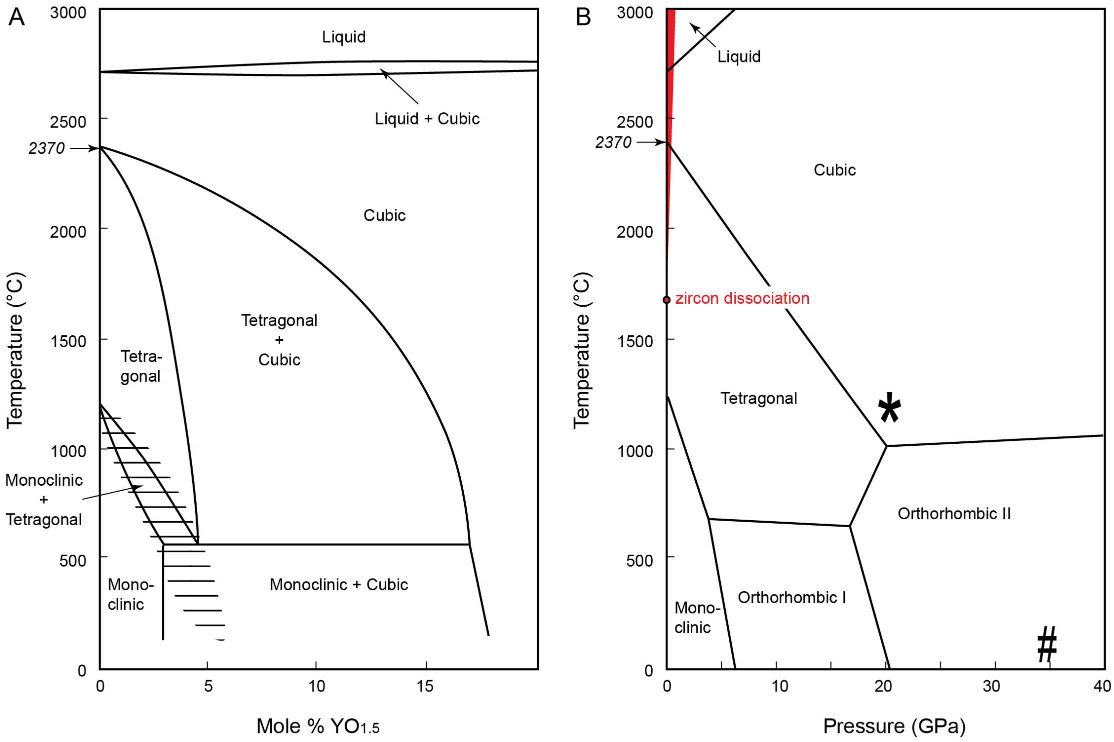

Figure S8. A. The effects of $YO_{1.5}$ impurities on the stability of ZrO_2 polymorphs, after Swab (2001). B. The effects of pressure on the stability of ZrO_2 polymorphs, after Bouvier et al. (2000) and references therein. The red dot and red shaded area show the conditions at which zircon dissociates to zirconia + silica after Kaiser et al. (2008) and Timms et al. (2017), respectively.

Item 8. Supplemental Reference List

Böhm, J., 1925. Über das Verglimmen einiger Metalloxyde. Zeitschrift für anorganische und allgemeine Chemie 149, 217-222.

Bondars, B., Heidemane, G., Grabis, J., Laschke, K., Boysen, H., Schneider, J., Frey, F., 1995. Powder diffraction investigations of plasma sprayed zirconia. Journal of Materials Science 30, 1621-1625.

Bouvier, P., Djurado, E., Lucazeau, G., Le Bihan, T., 2000. High-pressure structural evolution of undoped tetragonal nanocrystalline zirconia. Physical Review B 62, 8731-8737.

Cayron, C., 2007. ARPGE: a computer program to automatically reconstruct the parent grains from electron backscatter diffraction data. Journal of Applied Crystallography 40, 1183-1188.

Cayron, C., Douillard, T., Sibil, A., Fantozzi, G., Sao-Jao, S., 2010. Reconstruction of the Cubic and Tetragonal Parent Grains from Electron Backscatter Diffraction Maps of Monoclinic Zirconia. Journal of the American Ceramic Society 93, 2541-2544.

Downs, R.T., Palmer, D.C., 1994. The pressure behavior of c~-cristobalite. American Mineralogist 79, 9-14.

Farnan, I., Balan, E., Pickard, C.J., Mauri, F., 2003. The effect of radiation damage on local structure in the crystalline fraction of $ZrSiO_4$: Investigating the 29Si NMR response to pressure in zircon and reidite. American Mineralogist 88, 1663-1667.
Hazen, R.M., Finger, L.W., 1979. Crystal structure and compressibility of zircon at high pressure. American Mineralogist 64, 196-201.
Hill, R.J., Cranswick, L.M.D., 1994. International Union of Crystallography commission on powder difraction Rietveld refinement round robin. II. Analysis of monoclinic ZrO_2. Journal of Applied Crystallography 27, 802-844.
Kaiser, A., Lobert, M., Telle, R., 2008. Thermal stability of zircon ($ZrSiO_4$). Journal of the European Ceramic Society 28, 2199-2211.
Kirfe, A., Will, G., Arndt, J., 1979. A new phase of coesite SiO_2. Zeitschrift für Kristallographie 149, 315-326.
Prior, D.J., Boyle, A.P., Brenker, F., Cheadle, M.C., Day, A., Lopez, G., Peruzzo, L., Potts, G.J., Reddy, S., Spiess, R., Timms, N.E., Trimby, P., Wheeler, J., Zetterström, L., 1999. The application of electron backscatter diffraction and orientation contrast imaging in the SEM to textural problems in rocks. American Mineralogist 84, 1741-1759.
Sands, D.E., 1969. Introduction to crystallography. WA Benjamin, New York.
Swab, J., 2001. Role of oxide additives in stabilizing zirconia for coating applications. Army Research Laboratory, Aberdeen Proving Ground.
Teufer, G., 1962. The crystal structure of tetragonal ZrO_2. Acta Crystallographica 15, 1187.
Timms, N.E., Erickson, T.M., Pearce, M.A., Cavosie, A.J., Schmieder, M., Tohver, E., Reddy, S.M., Zanetti, M., Nemchin, A.A., Wittmann, A., 2017. A pressure-temperature phase diagram for zircon at extreme conditions. Earth Science Reviews 165, 185-202.
Zanetti, M.R., 2015. Investigating the Complexity of Impact Crater Ejecta, Department of Earth and Planetary Sciences. Washington University in St. Louis, Missouri, USA, St. Louis, Missouri, p. 218.